

12-2020

## Optimizing a Railroad Bearing Condition-Monitoring Algorithm for Use with an Onboard Wireless Low-Power Sensor Module

Jonas Regan Leano Cuanang  
*The University of Texas Rio Grande Valley*

Follow this and additional works at: <https://scholarworks.utrgv.edu/etd>



Part of the [Mechanical Engineering Commons](#)

---

### Recommended Citation

Cuanang, Jonas Regan Leano, "Optimizing a Railroad Bearing Condition-Monitoring Algorithm for Use with an Onboard Wireless Low-Power Sensor Module" (2020). *Theses and Dissertations*. 647.  
<https://scholarworks.utrgv.edu/etd/647>

This Thesis is brought to you for free and open access by ScholarWorks @ UTRGV. It has been accepted for inclusion in Theses and Dissertations by an authorized administrator of ScholarWorks @ UTRGV. For more information, please contact [justin.white@utrgv.edu](mailto:justin.white@utrgv.edu), [william.flores01@utrgv.edu](mailto:william.flores01@utrgv.edu).

OPTIMIZING A RAILROAD BEARING CONDITION-MONITORING ALGORITHM  
FOR USE WITH AN ONBOARD WIRELESS LOW-POWER  
SENSOR MODULE

A Thesis

by

JONAS REGAN LEANO CUANANG

Submitted to the Graduate College of  
The University of Texas Rio Grande Valley  
In partial fulfillment of the requirements for the degree of  
MASTER OF SCIENCE IN ENGINEERING

December 2020

Major Subject: Mechanical Engineering



OPTIMIZING A RAILROAD BEARING CONDITION-MONITORING ALGORITHM  
FOR USE WITH AN ONBOARD WIRELESS LOW-POWER  
SENSOR MODULE

A Thesis  
by  
JONAS REGAN LEANO CUANANG

COMMITTEE MEMBERS

Dr. Constantine Tarawneh  
Chair of Committee

Dr. Heinrich Foltz  
Co-chair of Committee

Dr. Arturo Fuentes  
Committee Member

December 2020



Copyright © 2020 Jonas Regan Leano Cuanang

All Rights Reserved



## ABSTRACT

Cuanang, Jonas Regan Leano, Optimizing a Railroad Bearing Condition-Monitoring Algorithm for Use with an Onboard Wireless Low-Power Sensor Module. Master of Science in Engineering (MSE), December 2020, 74 pp., 17 tables, 27 figures, 24 references

An algorithm that utilizes vibration measurements was developed by the UTRGV Center for Railway Safety to monitor the condition of railroad bearings. This algorithm uses the data collected from accelerometers on the bearing adapters to determine if there is a defect, where the defect is within the bearing, and the approximate size of the defect. Laboratory testing was performed on the UTCRS single bearing test rig. A four-second sample window of the recorded vibration data is used by the algorithm to reliably identify the defective component inside the bearing with up to a 100% confidence level. However, considerable computational power is used to analyze the 20,480 data points. Consequently, if this condition monitoring algorithm is to be implemented on a wireless module, the battery life becomes restricted. Reducing the sample window to one second of data collected would conserve energy but might sacrifice some accuracy in the analysis. To that end, a wireless onboard condition monitoring module that collects one second of vibration data (5,120 data points) was fabricated and tested to compare its efficacy against the existing wired setup. The study presented here demonstrates that the optimized algorithm for the wireless system can reliably identify the bearing condition with negligible compromise to accuracy and lower power consumption.





## DEDICATION

This thesis is dedicated to my loving family and to all the friends I have had the honor of meeting throughout the years. My mother, Anne, and father, Regan, for teaching me to work hard and to support me for pursuing a higher education. I would not be who I am, without any of you.



## ACKNOWLEDGEMENTS

I am truly grateful for my research advisor and mentor, Dr. Constantine Tarawneh. Your efforts in developing this research team and fostering your students for success is unmatched. I am very thankful to be accepted into your research team. I would not have seen myself grow this much as an engineer and person without you as my advisor.

I want to thank Dr. Arturo Fuentes for sparking my interest in vibrations. I would not be here if it were not for you.

I would also like to thank Dr. Heinrich Foltz for developing the wireless module and helping us out with troubleshooting the electrical components in our laboratory. The success of this project would not have been possible without your assistance.

To all my friends on the team, thank you for the laughs, encouragements, and adventures. Joseph, James, Javi, Anthony, thank you for teaching me everything I needed to know for this research. Charlie and Vero, I am glad to have gone through my graduate career with you two, it has been fun.

Finally, this study was made possible by funding provided by The University Transportation Center for Railway Safety (UTCRS), through a USDOT Grant No. #DTRT 13-G-UTC59.



## DISCLAIMER

The contents of this thesis reflect the views of the authors, who are responsible for the facts and the accuracy of the information presented herein. This document is disseminated under the sponsorship of the U.S. Department of Transportation's University Transportation Centers Program, in the interest of information exchange. The U.S. Government assumes no liability for the contents or use thereof.



## TABLE OF CONTENTS

	Page
ABSTRACT .....	iii
DEDICATION.....	iv
ACKNOWLEDGEMENTS.....	v
DISCLAIMER.....	vi
TABLE OF CONTENTS .....	vii
LIST OF TABLES .....	x
LIST OF FIGURES .....	xi
CHAPTER I.BACKGROUND AND INTRODUCTION .....	1
1.1 Freight Railcar Tapered-Roller Bearings .....	1
1.2 Wayside Bearing Condition Monitoring Systems .....	3
1.2.1 Trackside Acoustic Detection System (TADS <sup>TM</sup> ).....	3
1.2.2 RailBAM <sup>®</sup> .....	4
1.2.3 Hot-Box Detector (HBD).....	5
1.3 Investigation Reports on Overheated Bearings .....	6
1.3.1 Railway Investigation Report R11T0034 [15] .....	7
1.3.2 Railway Investigation Report R11T0016 [16] .....	8
1.4 Onboard Bearing Condition Monitoring Module .....	9
1.5 Wireless Utilization of the Developed Onboard Condition Monitoring Device .....	10
CHAPTER II.EXPERIMENTAL SETUP AND INSTRUMENTATION .....	11



2.1	Single Bearing Test Rig (SBT).....	11
2.2	Vibration and Temperature Sensors.....	13
2.3	Data Acquisition System.....	14
CHAPTER III.BEARING DEFECT DETECTION ALGORITHM .....		16
3.1	Defect Detection Algorithm .....	16
3.1.1	Level 1: Is the bearing defective?.....	17
3.1.2	Level 2: What is the defect type? .....	18
3.1.3	Level 3: What is the estimated defect size? .....	23
3.2	Optimizing the Defect Detection Algorithm .....	25
3.2.1	Zero Padding the Vibration Data.....	25
3.2.2	Windowing the Vibration Data.....	29
3.2.3	Normalized Defect Energy and the Hunting/Integration Ranges .....	30
CHAPTER IV.RESULTS AND DISCUSSION .....		31
4.1	Level 1: Is the Bearing Defective?.....	32
4.2	Level 2: What is the Defect Type? .....	33
4.2.1	Zero padding the vibration data.....	33
4.2.2	Applying a Hanning window function to the vibration data.....	35
4.2.3	Modifying the hunting and integration ranges .....	36
4.2.4	Modifying the normalized defect energy (NDE) calculations .....	44
4.2.5	Validation of the optimized algorithm for roller defects .....	50
CHAPTER V.CONCLUSIONS .....		52
REFERENCES .....		57

APPENDIX A.....	60
APPENDIX B.....	67
BIOGRAPHICAL SKETCH.....	74



## LIST OF TABLES

	Page
Table 1. Typical simulated railcar speeds used to perform the experiments for this study .....	13
Table 2. Corresponding defect type for each experiment .....	32
Table 3. Average vibration RMS values at 17% load.....	33
Table 4. Average vibration RMS values at 100% load.....	33
Table 5. Effectiveness of zero-padding on defect identification and its certainty.....	35
Table 6. Effect of using a Hanning window function on defect identification and its certainty ...	36
Table 7. Finding the optimal hunting ranges for zero-padding to 16,384 data points .....	38
Table 8. Finding the optimal hunting ranges for zero-padding to 32,768 data points .....	39
Table 9. Finding the optimal integration ranges for zero-padding to 16,384 data points .....	40
Table 10. Finding the optimal integration ranges for zero-padding to 32,768 data points .....	41
Table 11. Summary of the optimal hunting/integration ranges .....	42
Table 12. Optimizing the normalized defect energy calculations for 16,384 data points.....	45
Table 13. Optimizing the normalized defect energy calculations for 32,768 data points.....	45
Table 14. Summary of the optimal normalized defect energy calculations .....	46
Table 15. Level 2 analysis for 17% load (empty railcar) using the optimized algorithm.....	48
Table 16. Level 2 analysis for 100% load (full railcar) using the optimized algorithm .....	49
Table 17. Algorithm comparison of Level 2 analysis for a bearing containing roller defects .....	51



## LIST OF FIGURES

	Page
Figure 1. Basic components of a tapered-roller bearing [1] .....	1
Figure 2. Example of a localized defect (left) and a distributed defect (right).....	2
Figure 3. On-site Trackside Acoustic Detection System [6] .....	4
Figure 4. On-site RailBAM® system [9] .....	5
Figure 5. On-site Hot-Box-Detector (HBD) system [5].....	6
Figure 6. Map showing the path of the passenger train [15] .....	7
Figure 7. Diagram of the derailment site for CP freight train 220-24 [16].....	8
Figure 8. Burnt-off journal from railcar SKPX 622514 [16] .....	9
Figure 9. Single Bearing Test Rig (SBT) .....	12
Figure 10. Modified bearing adapter showing sensor locations .....	14
Figure 11. SBT thermocouple locations (red dots indicate the regular K-type thermocouple locations and black dots indicate the K-type bayonet thermocouple locations).....	14
Figure 12. Flow chart of the defect detection algorithm [18].....	17
Figure 13. Frequency spectrum plots (0 – 1000 Hz) of (a) a defect-free bearing, (b) outer ring ..	20
Figure 14. PSD plot that illustrates shifting of a cone defect frequency.....	21
Figure 15. Cup defect size correlation at 120 – 136 km/h and 100%/125% of full load [22].....	24
Figure 16. Cone defect size correlation at 120 – 136 km/h and 100%/125% of full load [22].....	24
Figure 17. Time and frequency domain plots of a 3 Hz signal .....	26
Figure 18. Time and frequency domain plots of a 3.5 Hz signal.....	27

Figure 19. Time and frequency domain plots of a 3.5 Hz signal zero-padded by 1,000 points ....	28
Figure 20. Time and frequency domain plots of a 3.5 Hz signal zero-padded by 9,000 points ....	28
Figure 21. Hanning window function applied to a 3.5 Hz signal zero-padded by 9,000 points ...	29
Figure 22. Algorithm speed for various zero-padding cases .....	35
Figure 23. A PSD plot of Experiment 228 with the fundamental defect frequencies and their harmonics shown.....	43
Figure 24. Algorithm speed comparing the wired accelerometer and the wireless module .....	49

## CHAPTER I

### BACKGROUND AND INTRODUCTION

#### 1.1 Freight Railcar Tapered-Roller Bearings

The suspension system that supports a freight railcar consists of side frames, springs, dampers, axles, wheels, and tapered-roller bearings. As a result of heavy cargo and high operational speeds, the bearings are the most susceptible to failure.

These bearings consist of three basic components that provide near-frictionless rotation in normal operation: inner ring (cone), outer ring (cup), and rollers, as shown in Figure 1. However, once a defect develops on one of these components, additional frictional heating usually ensues, which may cause the bearing temperature to rise depending on the defect size and location.



Figure 1. Basic components of a tapered-roller bearing [1]

Different defect types can be characterized as geometric defects, localized defects, or distributed defects. Geometric defects are components out of tolerance and can result from an



improper manufacturing process or abnormal operation of the bearing components. Examples of a localized defect (left) and distributed defect (right) are illustrated in Figure 2. Localized defects consist of pits, cracks, or spalls, while distributed defects are found on multiple bearing components with localized defects or a single component that has numerous localized defects distributed throughout its rolling surface. A water-etch component is one instance of a distributed defect where water enters the bearing through a broken seal and degrades the grease. The degraded lubricating properties of the grease lead to an increased metal-to-metal friction that causes the bearing components to wear out at a faster rate.

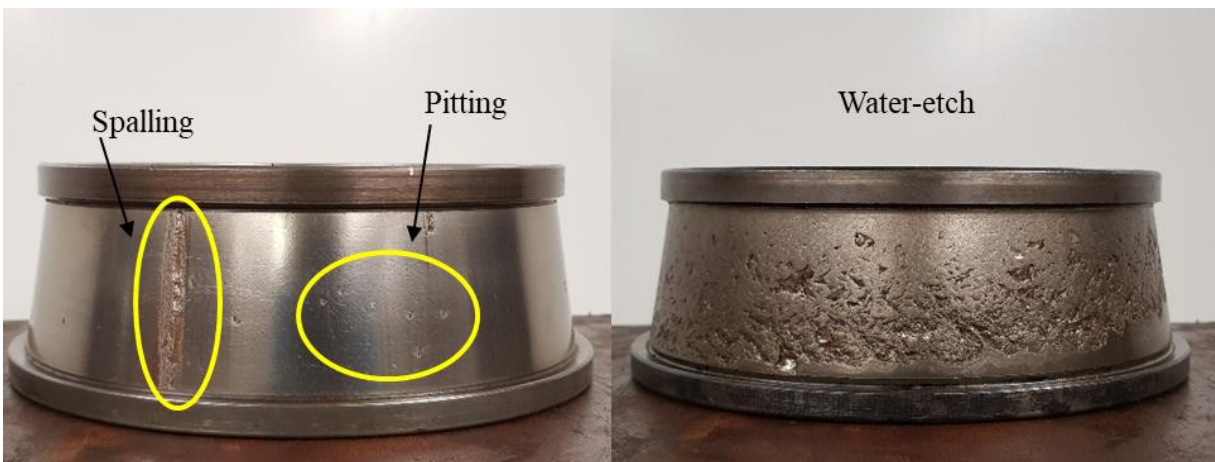


Figure 2. Example of a localized defect (left) and a distributed defect (right)

Pits, cracks, and spalls usually develop from subsurface inclusions that are within 400-600  $\mu\text{m}$  beneath the raceway surface. These subsurface inclusions develop from steel contaminants during the manufacturing process of the bearing components. Rolling contact fatigue (RCF) causes the subsurface inclusions to progress into localized defects. Constant RCF develops micro-cracks around the subsurface inclusions which would eventually propagate towards the raceway surface. Metal fragments are chipped away from the raceway surface which creates spalls, and the metal debris from the spall is circulated around the bearing through the grease to create dents and pits on the raceway surfaces [2, 3].

The nominal service life of a bearing is at least three million rail kilometers (two million rail miles) until it reaches failure by fatigue. Several bearing condition monitoring systems are utilized to identify bearings nearing failures.

## **1.2 Wayside Bearing Condition Monitoring Systems**

The most common bearing condition monitoring systems used in the railway industry are the Hot-Box Detectors (HBDs) and the Acoustic Bearing Detectors (ABDs). Both systems use wayside devices that are positioned adjacent to the rail tracks to monitor the condition of freight railcar bearings as they pass by these devices. If the data analyzed from a bearing exceeds a predetermined threshold for either monitoring system, the train conductor would be notified to stop, and the wheel-axle assembly with the defective bearing would be replaced.

### **1.2.1 Trackside Acoustic Detection System (TADS™)**

Shown in Figure 3, the TADS™ consists of multiple microphones on each side of the track that monitors bearing acoustic emissions from passing trains which would notify the train conductor if a specific bearing defect is severe enough for inspection. TADS™, initially, could detect smaller defects, but it quickly became apparent that it was costly to remove these low-risk defects with their remaining serviceable life span. As a result, the algorithm for the TADS™ was modified to identify high-risk bearings, such as a “growler”. Growlers emit a low frequency sound when about 90% of a bearing component’s raceway is spalled. However, a study determined that some high-risk bearings were not detected by the TADS™ [4]. With only 19 TADS™ systems in the nation (as of March 2017), most bearings in service are unlikely to pass through this system [5].



Figure 3. On-site Trackside Acoustic Detection System [6]

### 1.2.2 RailBAM®

The RailBAM®, shown in Figure 4, is another bearing acoustic detector that uses a set of wayside microphones to identify early and advanced defects. The distinct feature that separates the RailBAM® from the TADS™ is its capability to provide a predictive trend of the bearing severity [7]. A trend is created for a bearing's acoustic history every time the train passes by this device. This allows the railcar owner to optimally create a systematic maintenance plan to reduce costly inspections. However, a small percentage of railcars would pass through this system as there are only 20 RailBAM® devices (as of March 2017) populated in the East and Midwest locations of the United States [5, 8].



Figure 4. On-site RailBAM® system [9]

### 1.2.3 Hot-Box Detector (HBD)

With over 6,000 units in North America, Hot Box Detectors (HBDs) are the most common bearing condition monitoring systems, typically placed within 40 km (25 miles) to 64 km (40 miles) apart [8]. HBDs utilize non-contact infrared sensors to measure the emitted temperature from railcar bearings, wheels, axles, and brakes. Bearings operating at temperatures that exceed  $94.4^{\circ}\text{C}$  ( $170^{\circ}\text{F}$ ) above the ambient temperature or are  $58.3^{\circ}\text{C}$  ( $105^{\circ}\text{F}$ ) hotter than their axle mate bearing will trigger an alarm that alerts the train conductor and results in the removal of the suspect bearing from service [10]. Some railroads use a more conservative method that scans for “warm trending” bearings. These are bearings operating at temperatures that are significantly above the average temperature of all bearings on the same side of the train [10]. This approach would have the warm-trended bearings later removed for inspection without triggering any HBD alarms. Despite the large number of HBDs deployed, train derailments caused by overheated bearings still occur.



Figure 5. On-site Hot-Box-Detector (HBD) system [5]

### **1.3 Investigation Reports on Overheated Bearings**

The accuracy and reliability of HBD temperature sensors have been investigated through a number of laboratory and field studies [11, 12, 13]. It was determined that the operating bearing temperature can be inaccurately measured by the HBD's infrared sensors. Reasons for erroneous measurements include the railroad bearing class, its location on the axle, and harsh environmental effects. From 2010 to 2020, 146 train derailments caused by overheated bearings resulted in damages over \$50 million in the United States and Canada. In all these cases, the HBDs failed to detect these severely defective bearings [14]. As mentioned earlier, several railroads ran statistical analysis on the data acquired from HBDs seeking warm-trending bearings in service operation. These bearings were later removed from service, and a visual inspection was performed to determine the cause of their abnormal temperature behavior. A study conducted by Amsted Rail engineers found that about 40% of bearings removed from service for warm trending between 2001 and 2007 contained no noticeable defects. These bearings were

categorized as non-verified since the reason behind their abnormal temperature behavior could not be determined. Non-verified bearings are a major concern as they result in costly train stoppages and delays that disrupt freight rail service.

### 1.3.1 Railway Investigation Report R11T0034 [15]

On February 6, 2011, a passenger train that occupied 106 passengers and 5 crew members started its designation from London, Ontario to Toronto, Ontario around 7:40 a.m. E.S.T. Less than two hours later, illustrated in Figure 6., the train passed through a HBD in the Oakville Subdivision without triggering any alarms. One bearing on a coach VIA 4009 railcar was found to run hotter than the average temperature of all bearings, but its temperature never reached the critical HBD threshold. While the train was scheduled for a stop in Oakville, the stationmaster noticed smoke coming from the bearing in the R4 location on the coach VIA 4009 railcar. The bearing was stated to have overheated and failed without being detected by an HBD.

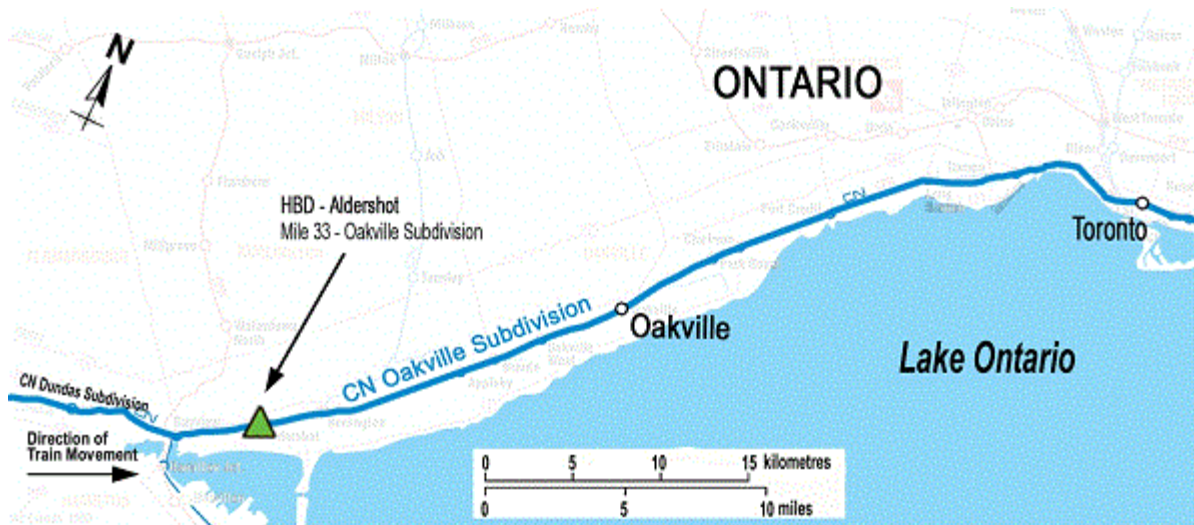


Figure 6. Map showing the path of the passenger train [15]

After removing the overheated bearing from service, further inspection was mandated to find its cause of failure. Several conclusions from the disassembly were made: the bearing was manufactured in 1979; bearing components were heat tinted and deformed; spalls were present

on the cup and cone; and the rollers, cage, and seals were unsalvageable. Finding the exact cause of failure was not possible due to the severe damages, but speculation suggests that component spalling caused the bearing to overheat and fail.

### 1.3.2 Railway Investigation Report R11T0016 [16]

Canadian Pacific Railway (CP) freight train 220-24 departed Sudbury, Ontario on January 25, 2011 to deliver cargo to Toronto, Ontario. The train passed through eight HBDs in the Bala Subdivision without triggering any alarms. However, four of the last five HBDs indicated that railcar SKPX 625514 had warm-trending bearings. The next day, around 3:10 a.m. E.S.T., railcar SKPX 622514 had derailed while the train was traveling at 72 km/h (45 mph). The train continued for approximately one mile until another 20 railcars derailed and collided with CP freight train 221-25 that was stopped adjacent to the main track. A diagram of the derailment site is illustrated in Figure 7.

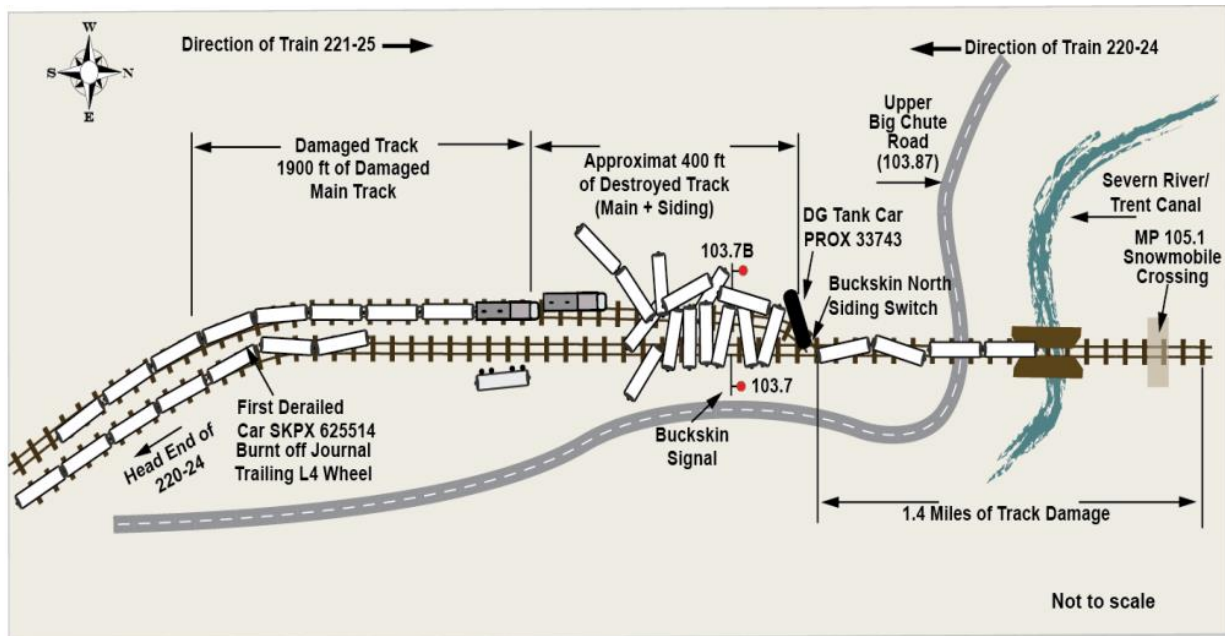


Figure 7. Diagram of the derailment site for CP freight train 220-24 [16]

Upon inspection of the wheelsets from the first railcar that derailed (SKPX 622514), the bearing from the L4 location was found to have burnt off on the axle. Shown in Figure 8, the burnt-off journal was heat tinted, deformed, and had a severe spall on the inboard cup raceway. The large cup defect had caused the bearing to overheat and burn off.



Figure 8. Burnt-off journal from railcar SKPX 622514 [16]

#### **1.4 Onboard Bearing Condition Monitoring Module**

Findings from current wayside condition monitoring systems indicate that the number of deployed ABDs are not sufficient to cover the railway system in North America, and that bearings can fail between HBD locations. Researchers from the University Transportation Center for Railway Safety (UTCRS) at the University of Texas Rio Grande Valley (UTRGV) conducted a study that compared the temperature profiles of defect-free (healthy) bearings to bearings with defects either on the cup or cone raceways [17]. The results concluded that healthy and defective bearings had similar operating temperatures, indicating that temperature alone is not a good prognostic for the bearing condition [17].

The shortcomings of the wayside condition monitoring systems prompted UTCRS researchers to start the development of an onboard device that continuously evaluates the health



of a bearing via both vibration and temperature measurements. The developed device can predict the deterioration rate of a bearing's raceway, which can allow the bearing to remain in service for a longer time span. The reliability of this device in accurately detecting defective bearings has been validated through numerous laboratory experiments at UTRGV and a three-day field test carried out using the test tracks at the Transportation Technology Center, Inc. (TTCI) in Pueblo, Colorado.

### **1.5 Wireless Utilization of the Developed Onboard Condition Monitoring Device**

The existing onboard condition monitoring device utilizes a wired system to analyze four seconds of vibration data (20,480 data points). However, a field implementation of this wired system is not feasible, so a wireless version of this device must be created. Although the wired system has sufficient computational power to analyze large sample windows of vibration data, it is a main concern to conserve the battery life of an onboard wireless device. Reducing the amount of data necessary to perform an accurate and reliable assessment of the bearing health will have major implications on the power consumption and battery life of the developed wireless onboard condition monitoring device. The algorithm used to monitor bearing condition has a three-step analysis process. Level 1 analysis determines if the bearing is healthy or defective; Level 2 analysis identifies the bearing defective component; and Level 3 analysis estimates the size of the defect. Therefore, optimizing the algorithm to effectively run the three analyses using a one-second data sample window will make the implementation of the wireless onboard condition monitoring device possible.

The study reported in this thesis will focus on the optimization of the developed onboard condition monitoring device for wireless utilization to reduce computational power and battery consumption while still maintaining accurate assessments of the bearing condition.

## CHAPTER II

### EXPERIMENTAL SETUP AND INSTRUMENTATION

#### 2.1 Single Bearing Test Rig (SBT)

The University Transportation Center for Railway Safety (UTCRS) at UTRGV possesses a dynamic Single Bearing Test Rig (SBT), pictured in Figure 9, that can accommodate one class K (6½"×9"), class F (6½"×12"), class G (7"×12"), or class E (6×11") tapered-roller bearings. The tester configuration has the test bearing cantilevered at the end of the axle to closely replicate the loading conditions of freight railcar bearings in service.

According to the Association for American Railroads (AAR) standards, full load on railcar bearings of class F or K is rated at 153 kN (34.4 kips) per bearing. The SBT is equipped with a hydraulic cylinder that can apply vertical loads up to 150% of full load. The experimental data presented in this thesis were acquired utilizing two freight railcar loading conditions: 153 kN (34.4 kips) per bearing which corresponds to a fully loaded railcar (i.e., 100% load), and 17% of full load which simulates an empty railcar. A calibrated load cell with an accuracy of 0.5% over its operating range was used to accurately measure and record the load applied to the test bearing. An Arduino-based load controller is used to automatically adjust the applied load within a 1% tolerance to counteract the effects of thermal expansion and contraction of the hydraulic oil in the load cylinder. Railcar speeds based on a traditional 36-inch wheel, which are listed in Table 1, can be replicated using a 22 kW (30 hp) variable frequency motor. The SBT can simulate wheel impact forces up to 222 kN (50 kips) that are caused by defective wheels or poor

track conditions. Moreover, the SBT is also equipped with a lateral load cylinder that can apply a lateral load to the bearing up to 22 kN (5 kips) to mimic forces that a bearing may experience while the railcar is navigating a curved portion of rail track.

An average air stream of 5 m/s (11.2 mph) is produced from two industrial size fans that are used to provide convection cooling around the test bearing similar to what bearings in service experience. Apart from air cooling the test bearing, the two pillow block support bearings are water-cooled utilizing an industrial chiller to prevent them from overheating during experimental testing. In this study, testing performed using defective bearings containing spall(s) on the cup (outer ring) raceway were positioned such that the spalled region of the cup was directly under the full applied load to simulate a worst-case scenario where the defect can propagate as fast as possible.

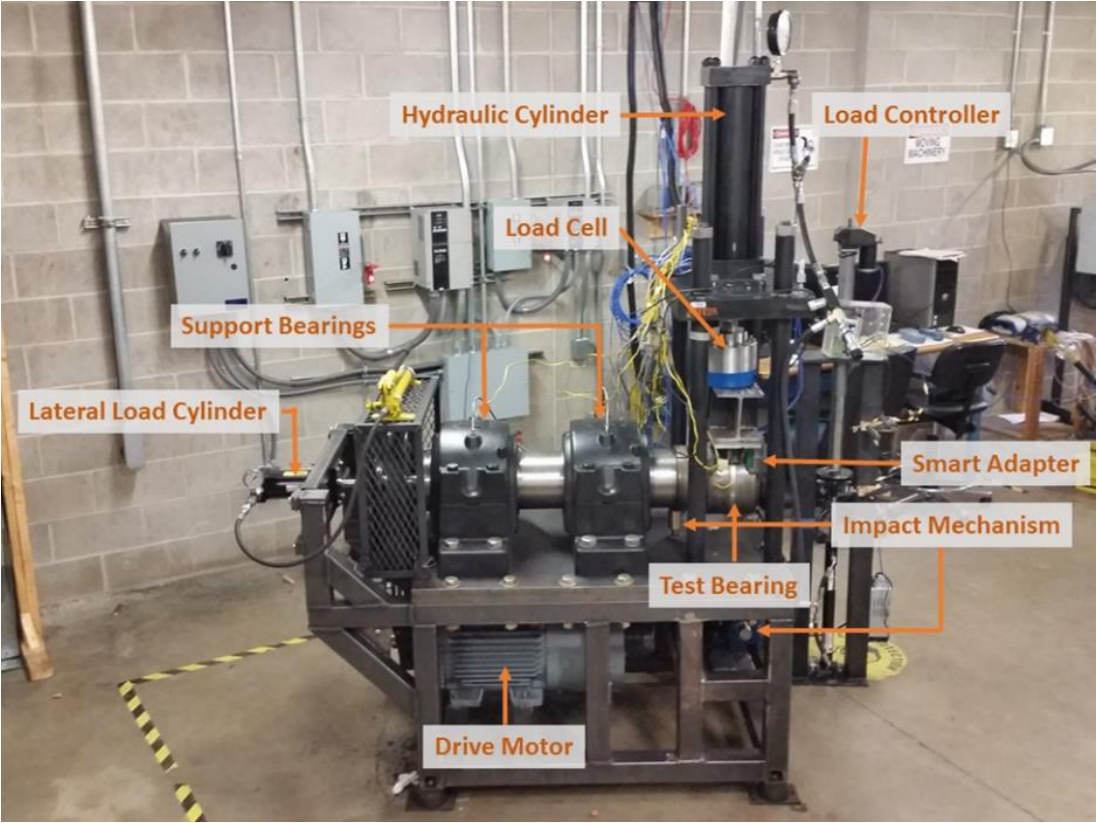


Figure 9. Single Bearing Test Rig (SBT)

Table 1. Typical simulated railcar speeds used to perform the experiments for this study

<b>Axle Speed [rpm]</b>	<b>Track Speed [mph]</b>	<b>Track Speed [km/h]</b>
420	45	72
467	50	80
498	53	85
560	60	97
618	66	106

## 2.2 Vibration and Temperature Sensors

A bearing adapter was machined to accommodate two 100g ADI accelerometers, one 70g ADI accelerometer, one 500g PCB accelerometer, and a custom wireless onboard condition monitoring sensor module, as pictured in Figure 10. Referring to that figure, the two wired 100g accelerometers were mounted at the Smart Adapter™ (SA) and Mote (M) locations on the inboard side of the bearing. The outboard side of the bearing has one wired 70g accelerometer and a wireless sensor module that utilizes a 100g accelerometer mounted on the SA location, and a 500g PCB accelerometer mounted on the Radial (R) location. A battery pack that powers the wireless sensor module was affixed on the outboard M location. The bearing adapter is also retrofitted with four K-type spring-loaded bayonet thermocouples to monitor the bearing temperatures on the inboard and outboard raceways. An additional seven K-type thermocouples, held tightly by a hose clamp, surround the circumference of the bearing cup to measure its surface temperature. Figure 11 indicates the thermocouple locations on the test bearing.

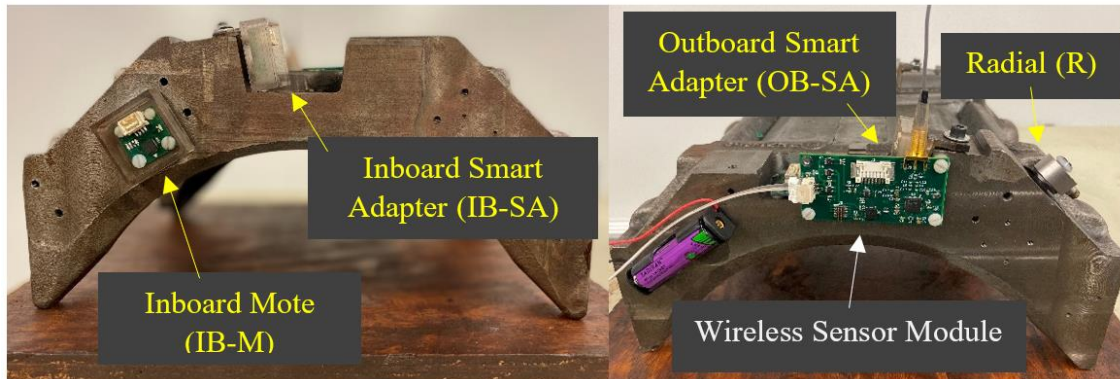


Figure 10. Modified bearing adapter showing sensor locations

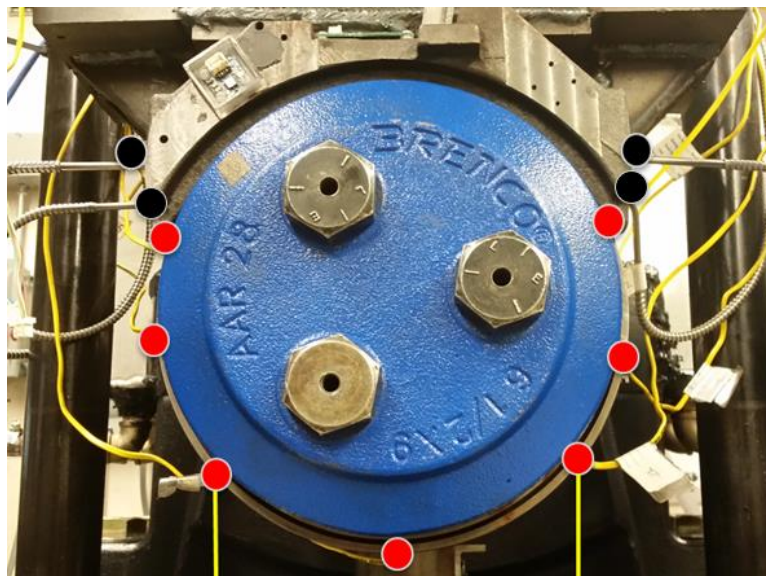


Figure 11. SBT thermocouple locations (red dots indicate the regular K-type thermocouple locations and black dots indicate the K-type bayonet thermocouple locations)

### 2.3 Data Acquisition System

LabVIEW™ was programmed to collect and record data from a National Instruments (NI) PXIe-1062Q data acquisition system (DAQ). Thermocouples were used to collect half second sample windows of the temperatures around the bearing every twenty seconds at a 128 Hz sampling rate using a NI TB-2627 card. Each half second sample window of temperature data

was average to produce one temperature data point. This process was implemented for each thermocouple.

An 8-channel NI PXI-4472B card was used to collect sixteen seconds worth of data every ten minutes from the wired accelerometers at a 5.12 kHz sampling rate. For the wireless sensor module, only one second of accelerometer data was acquired at a 5.20 kHz sampling rate every ten minutes. The data was transmitted via Bluetooth to a Raspberry Pi 3 Model B+. The collected data was then analyzed using MATLAB™ to calculate the root-mean-square (RMS) values and frequency spectrums of the bearing vibration signatures.

## CHAPTER III

### BEARING DEFECT DETECTION ALGORITHM

#### 3.1 Defect Detection Algorithm

Gonzalez [18] developed a preliminary bearing defect detection algorithm that identifies whether there is a defect in a bearing raceway, the location of the bearing defect, and the estimated size of the defect. This algorithm was optimized to work with a wired accelerometer module affixed to a bearing adapter and collects four seconds of vibration data at a 5.12 kHz sampling rate (20,480 data points). The root-mean-squared (RMS) values of the vibration data are calculated, and the corresponding frequency spectrums are then analyzed to assess the health of bearings. Figure 12 presents a three-step process flowchart of the defect detection algorithm that was developed for field service implementation. In this version, the algorithm is triggered when the train travels with speeds at or above 65 km/h (40 mph) or when the bearing operating temperature reaches 93°C (200°F). These thresholds can be easily adjusted through programming and are only meant to minimize power consumption by not having the sensor module awake all the time. The frequency of data collection can be optimized to save on power consumption, which is one of the areas of improvement in the work presented here.

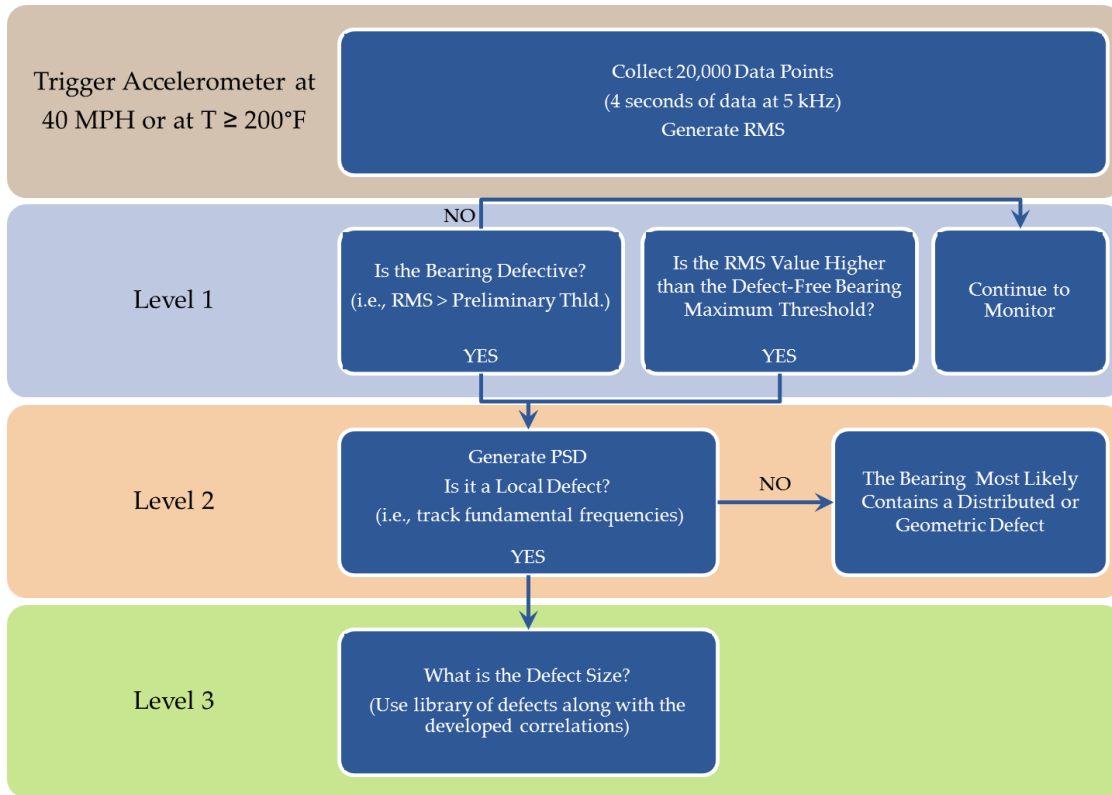


Figure 12. Flow chart of the defect detection algorithm [18]

The three levels of analysis presented in the flowchart of Figure 12 are briefly described hereafter.

### 3.1.1 Level 1: Is the bearing defective?

The first step of the algorithm determines whether the bearing is healthy or defective. The vibration RMS values from the bearing are compared against two speed-dependent thresholds. These thresholds were developed from sixty-two laboratory experiments that collected the vibration data of defect-free (healthy) bearings.

#### 3.1.1.1 Preliminary Threshold ( $T_p$ )

The “Preliminary Threshold ( $T_p$ )” was developed from a statistical analysis of several possible thresholds that are based on the correlation between railcar speed ( $V$ ) and the mean RMS vibration values of defect-free bearings. The ideal  $T_p$  should limit the number of defect-free



bearings above the threshold while minimizing the amount of defective bearings below the threshold. The selected  $T_p$  is provided in Eq. (1) [18].

$$\begin{aligned}
 T_p &= 7.331 \times 10^{-2} \times V [km/h] - 9.059 \times 10^{-2} \\
 T_p &= 4.556 \times 10^{-2} \times V [mph] - 9.059 \times 10^{-2} \\
 T_p &= 4.879 \times 10^{-3} \times V [rpm] - 9.059 \times 10^{-2}
 \end{aligned} \tag{1}$$

Bearings with RMS values that are below the  $T_p$  are considered to be defect-free (healthy), and the algorithm continues to monitor the vibration data. If the bearing RMS values are above the  $T_p$ , the bearing is tagged as possibly defective, and the algorithm advances to Level 2 analysis.

### 3.1.1.2 *Maximum Threshold ( $T_{max}$ )*

The “Maximum Threshold ( $T_{max}$ )” is based on a statistical analysis of the correlation between railcar speed ( $V$ ) and the maximum RMS vibration values at each speed. This analysis provides a conservative approach where bearings with RMS values above the  $T_{max}$  are categorized as defective. The  $T_{max}$  is given by Eq. (2) [18].

$$\begin{aligned}
 T_{max} &= 1.788 \times 10^{-1} \times V [km/h] - 1.008 \\
 T_{max} &= 1.111 \times 10^{-1} \times V [mph] - 1.008 \\
 T_{max} &= 1.119 \times 10^{-2} \times V [rpm] - 1.008
 \end{aligned} \tag{2}$$

### 3.1.2 **Level 2: What is the defect type?**

This step in the algorithm determines the defect type (local or distributed/geometric) of the identified defective bearing by analyzing the power spectral density (PSD) plots. Given in Eq. (3), the PSD is the square of the magnitudes in the frequency domain. The PSD plots are used to analyze the six fundamental rotational frequencies of a tapered-roller bearing that are represented by Eq. (4) – Eq. (9) [20].

$$PSD = |X(f)|^2 \quad (3)$$

$$\omega_{cone} = \omega_o \quad (4)$$

$$\omega_{cage} = \left( \frac{R_{cone}}{R_{cone} + R_{cup}} \right) \omega_{cone} \quad (5)$$

$$\omega_{roller} = \left( \frac{R_{cone}}{D_{roller}} \right) \omega_{cone} \quad (6)$$

$$\omega_{out} = 23\omega_{cage} \quad (7)$$

$$\omega_{in} = 23(\omega_{cone} - \omega_{cage}) \quad (8)$$

$$\omega_{rolldef} = \left( \frac{R_{cup}}{R_{roller}} \right) \omega_{cage} \quad (9)$$

These frequencies are based on the axle rotational speed ( $\omega_o$ ) and the component geometries of a tapered-roller bearing.  $R_{cone}$ ,  $R_{cup}$ , and  $R_{roller}$  denote the radii of the cone (inner ring), cup (outer ring), and roller components, respectively, while the diameter of the roller is denoted as  $D_{roller}$ . The fundamental frequencies of the cone/axle, cage, and roller are represented by Eq. (4) – Eq. (6), respectively, while Eq. (7) – Eq. (9) give the fundamental defect frequencies of a defective cup (outer ring), cone (inner ring), and roller, respectively. Calculating these fundamental frequencies is imperative to correctly identify the type of defect within the bearing. A PSD plot that shows a peak in power at a corresponding defect frequency signifies that the bearing component is defective. PSD plots of defect-free bearings would contain no significant peaks in power. Figure 13 presents PSD plots for a healthy (defect-free) bearing as compared to bearings with a cup, cone, and roller defect, respectively. The fundamental defect frequencies are given in the plots, and the red vertical lines in Figure 13 represent the harmonics of each defect frequency.

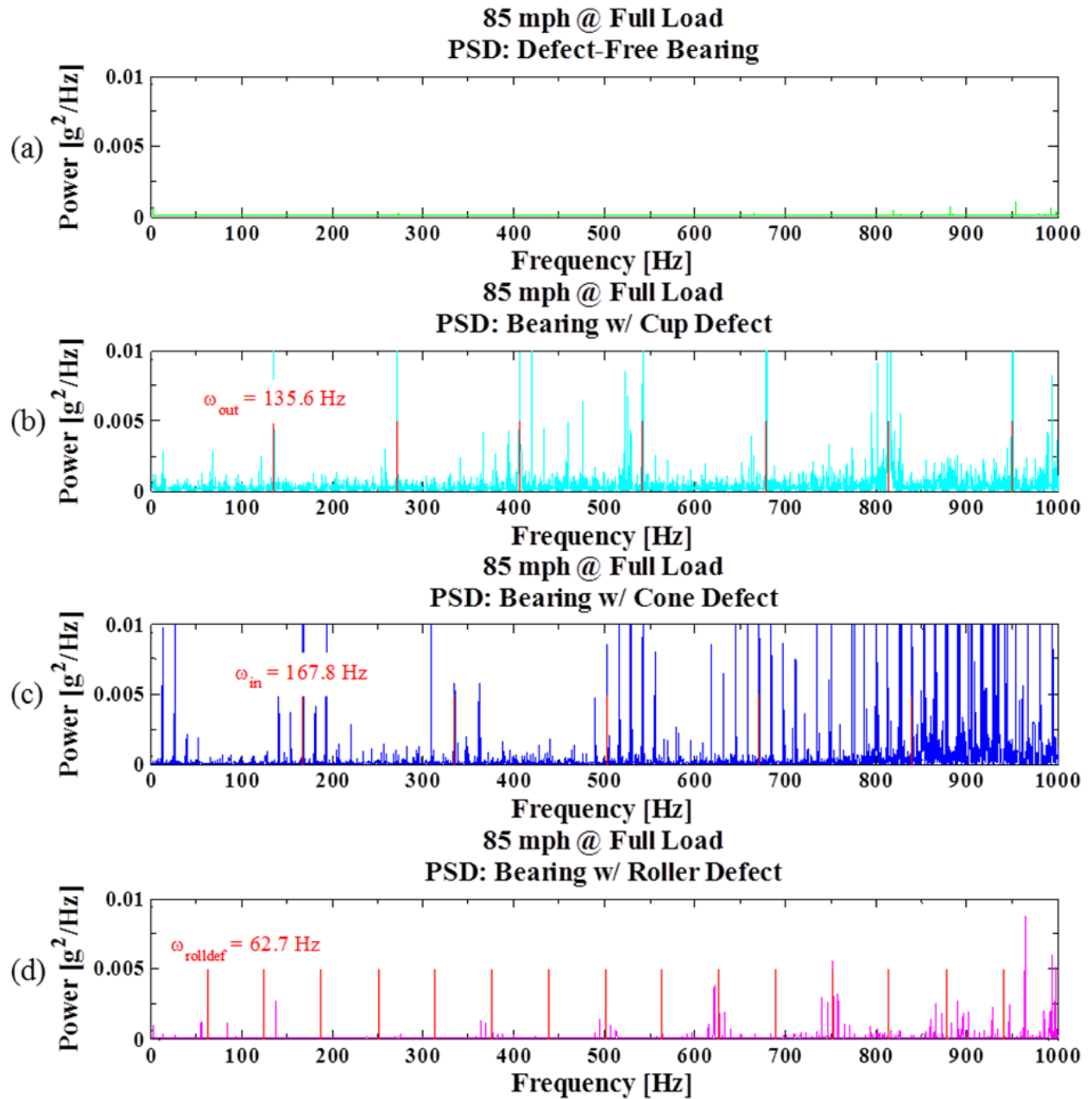


Figure 13. Frequency spectrum plots (0 – 1000 Hz) of (a) a defect-free bearing, (b) outer ring defect, (c) inner ring defect, and (d) a roller defect [19]. The red vertical lines represent the harmonics of each defect frequency.

Due to the different characteristics of each defect type in the PSD plots, Alvarado [21] developed a numerical method that calculated the normalized defect energy (NDE) for each defect type based on the fundamental defect frequencies and their harmonics. The NDE is the

summation of areas under the corresponding fundamental defect frequency (cup, cone, or roller) and its harmonics divided by the total number of harmonics within a specified frequency range. This method is used to classify the defect type. However, laboratory testing concluded that roller slipping within the cone assembly or small variations in the component tolerances can cause the calculated defect frequencies to slightly deviate from the actual defect frequencies resulting in incorrect NDE values. This phenomenon is illustrated in Figure 14 and is resolved by applying an appropriate hunting range ( $h_r$ ) where the algorithm looks for the actual defect frequency within that range. Note that the actual fundamental defect frequency is the highest peak within the chosen hunting range.

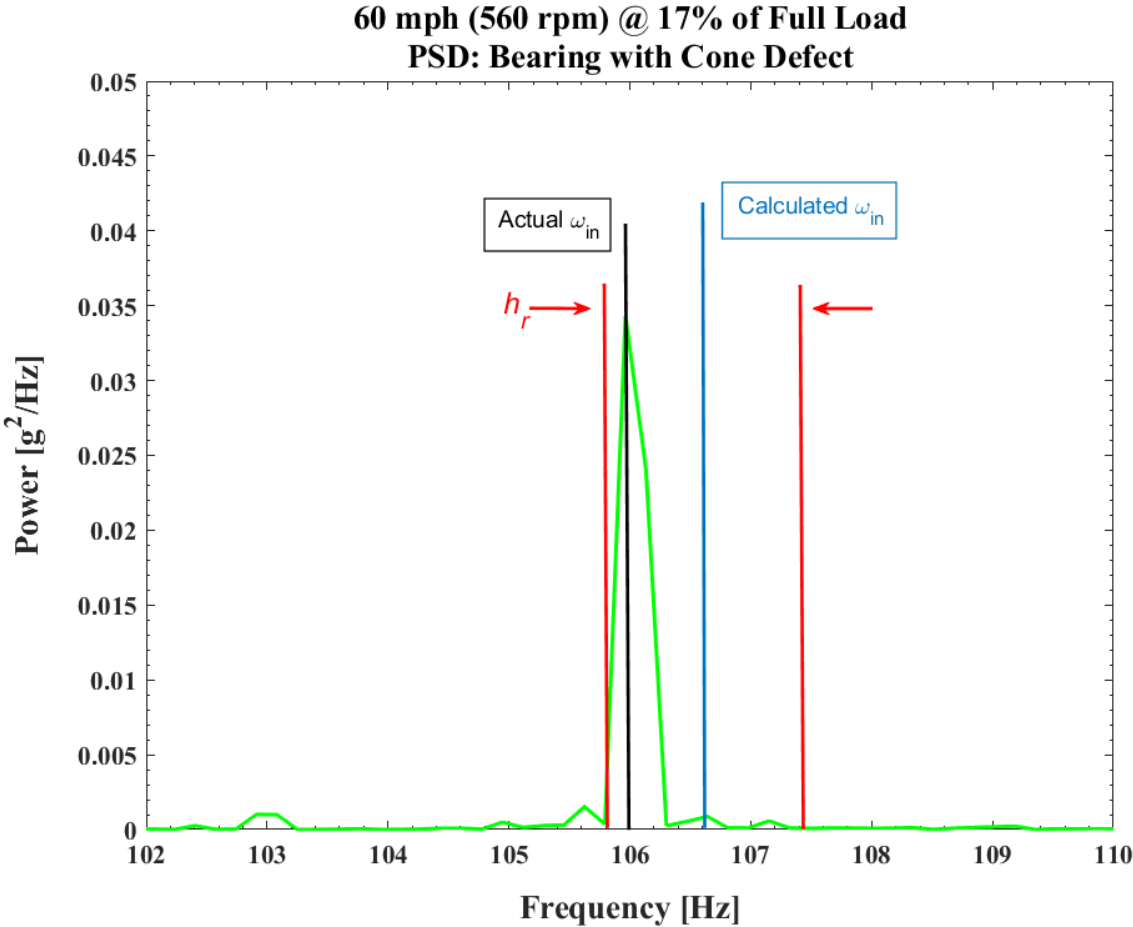


Figure 14. PSD plot that illustrates shifting of a cone defect frequency

The hunting range ( $h_r$ ) is a function of the frequency-bin resolution ( $rs$ ) and varies with the bearing's rotational speed. The frequency-bin resolution ( $rs$ ) is defined as the sampling frequency divided by the number of data points used in the frequency spectrum. The preliminary hunting ranges are given for three distinct rotational speed ranges as follows:

$$\text{Low Speed:} \quad \omega_o < 350 \text{ rpm}, h_r = \pm rs \times 6$$

$$\text{Medium Speed:} \quad 350 \text{ rpm} \leq \omega_o < 610 \text{ rpm}, h_r = \pm rs \times 10$$

$$\text{High Speed:} \quad 610 \text{ rpm} \leq \omega_o, h_r = \pm rs \times 15$$

Once the actual fundamental defect frequencies are found, the normalized defect energies can be calculated. The normalized defect energy (NDE) for each defect type are computed using Eq. (10) – Eq. (12). To ensure that the entire area under the defect frequency and its harmonics is captured, an integration range ( $i_r = rs \times 3$ ) was utilized so that accurate normalized defect energies can be calculated for the specified frequency range. In Eq. (10) – Eq. (12), the variable  $n$  represents the total number of harmonics of each fundamental defect frequency within the desired frequency range.

$$NDE_{cup} = \frac{\sum_{i=1}^n \int_{i\omega_{out}-i_r}^{i\omega_{out}+i_r} |X(f)|^2 df}{n} \quad (10)$$

$$NDE_{cone} = \frac{\sum_{i=1}^n \int_{i\omega_{in}-i_r}^{i\omega_{in}+i_r} |X(f)|^2 df}{n} \quad (11)$$

$$NDE_{roller} = \frac{\sum_{i=1}^n \int_{i\omega_{rolldef}-i_r}^{i\omega_{rolldef}+i_r} |X(f)|^2 df}{n} \quad (12)$$

The defect type is then identified through Eq. (13). In this equation, the algorithm compares the three NDEs calculated by Eq. (10) – Eq. (12), and then divides the greatest of the three NDEs by the sum of all three NDEs. A 50% minimum ratio of the greatest NDE to the sum of the three defect NDEs indicates a local defect corresponding to the maximum NDE of cup,

cone, or roller. Ratios that fall below the 50% criterion signify that the bearing may either contain a geometric defect, a distributed defect on multiple bearing components, or the bearing was falsely identified as defective (not common). Once a localized defect that meets the 50% criterion is detected, the algorithm advances to Level 3 analysis.

$$\frac{\max (NDE_{cup,cone,roller})}{NDE_{cup} + NDE_{cone} + NDE_{roller}} \times 100 \geq 50\% \quad (13)$$

### 3.1.3 Level 3: What is the estimated defect size?

After identifying the defective component in the Level 2 analysis, Level 3 analysis approximates the area of the defect. This predictive method was developed through correlations between the vibration RMS values and the corresponding defect areas. Correlations were only devised for cup (outer ring) and cone (inner ring) defects since roller defects are not that common and are mostly caused by interaction with defective cups and/or cones. The developed cup and cone correlations have undergone several optimizations over the past decade as more data was generated through continued laboratory testing yielding better and more accurate results that represent a wider range of defect areas. The most recent defect size correlations for cup and cone defects are provided in Figure 15 and Figure 16, respectively [22].

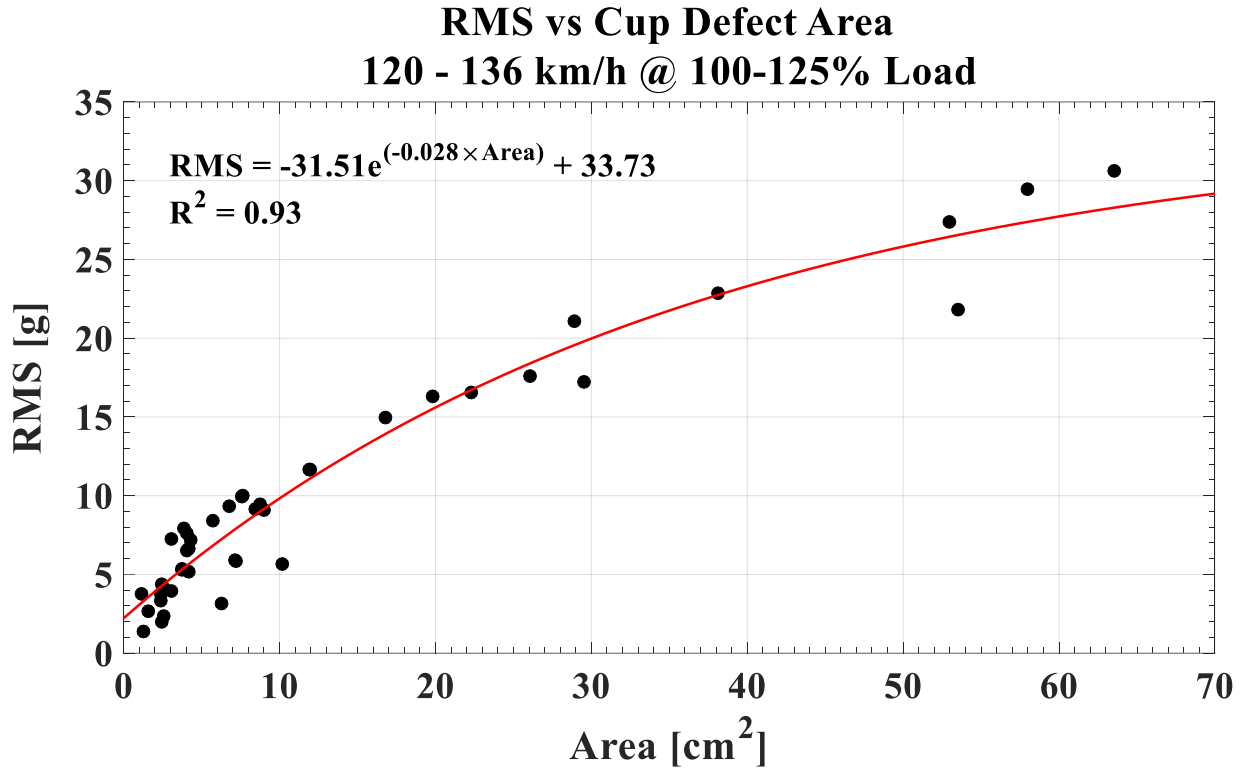


Figure 15. Cup defect size correlation at 120 – 136 km/h and 100%/125% of full load [22]

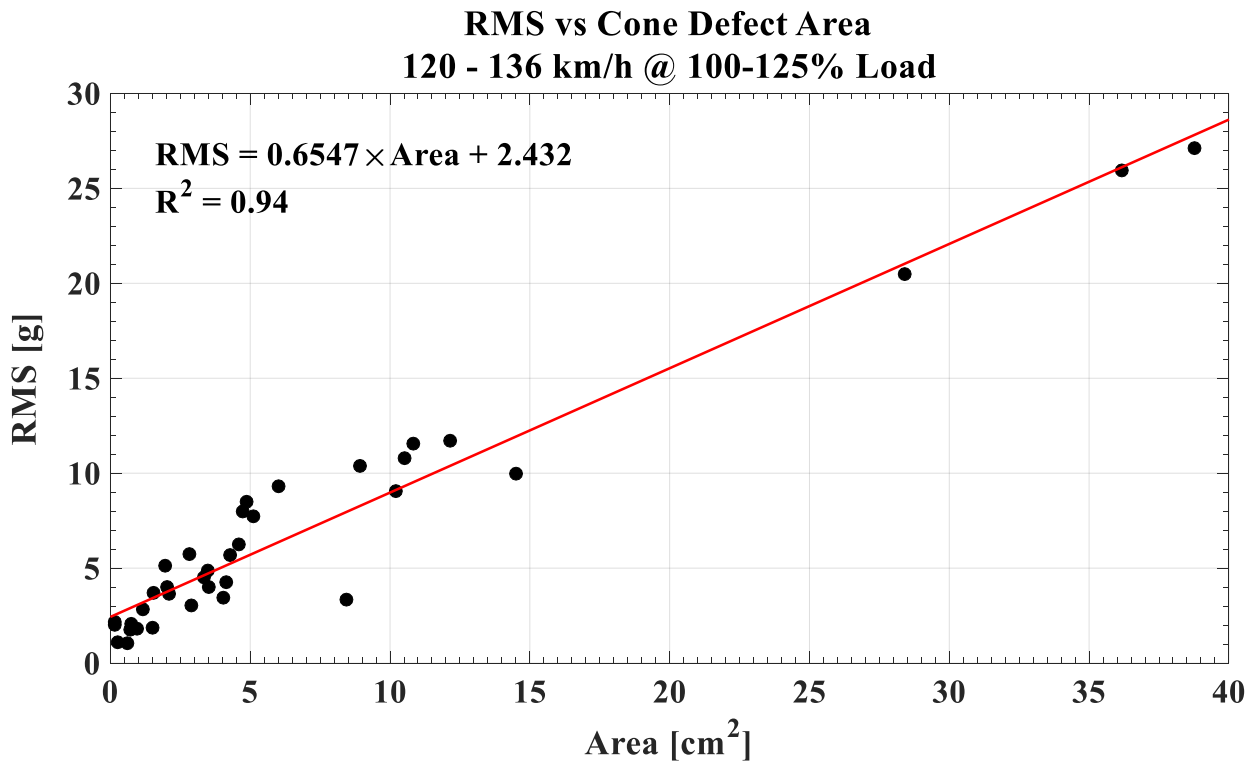


Figure 16. Cone defect size correlation at 120 – 136 km/h and 100%/125% of full load [22]

## **3.2 Optimizing the Defect Detection Algorithm**

A four second sample window of the recorded vibration data is used by the algorithm to reliably identify the defective component inside the bearing up to a 100% confidence level for a wired accelerometer. However, considerable computational power is used to analyze the 20,480 data points. Consequently, if this condition monitoring algorithm is to be implemented on a wireless module, the battery life becomes restricted. Reducing the sample window to one second of data would conserve energy but might sacrifice some accuracy in the analysis. To that end, a wireless onboard condition monitoring module that collects one second of vibration data (5,200 data points) was fabricated and tested to compare its efficacy against a wired setup. Note that implementing a wired system in freight rail service is not feasible, which underscores the importance of optimizing the defect detection algorithm for wireless sensor implementation.

### **3.2.1 Zero Padding the Vibration Data**

Since a smaller sample window of the vibration data is collected with the wireless module, several optimizations of the algorithm were considered to accurately assess the health of bearings. Figure 17 shows the time and discrete Fourier transform (DFT) plots of a one second window of a 3 Hz sinusoid that was sampled at 1 kHz. The DFT plot of this signal shows a magnitude that is only present at 3 Hz, which is also the frequency of the signal. However, if we try to analyze a signal with a frequency of 3.5 Hz at the same sampling frequency and sample window, the DFT plot, shown in Figure 18, does not show the correct magnitude that should only appear at 3.5 Hz. This occurs because the resolution (the sampling rate divided by the number of points in the DFT) of this signal is 1 Hz, which is too coarse to find the 3.5 Hz signal. Since the frequency of the signal cannot be resolved, spectral leakage occurs and energy from the unresolved frequency is dispersed throughout the whole spectrum. Spectral leakage is unwanted



because frequency bins throughout the whole spectrum result in larger magnitudes. However, as the resolution approaches the order of the signal frequency, the significance of spectral leakage decreases.

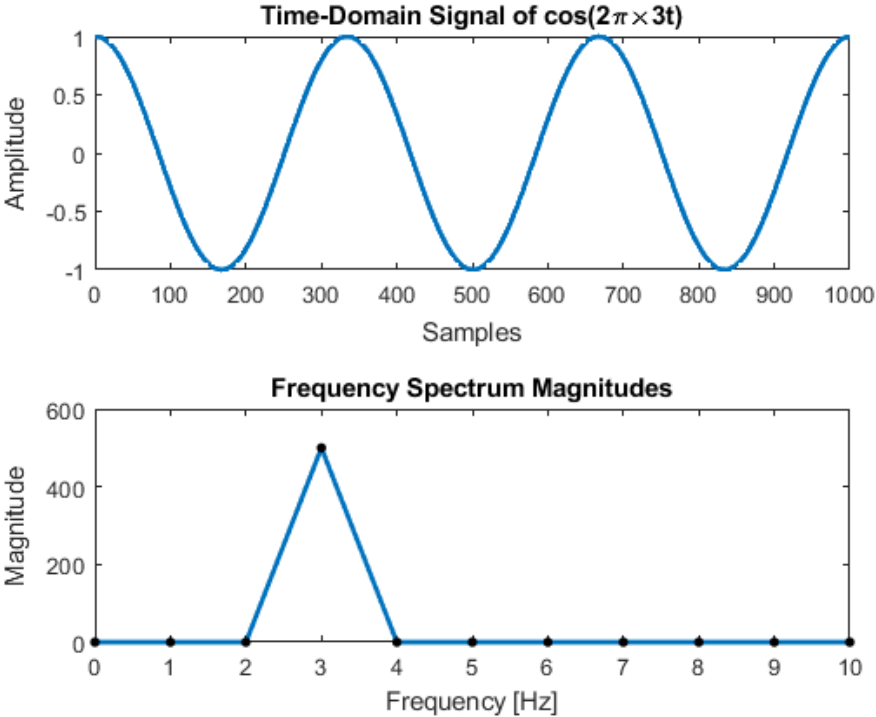


Figure 17. Time and frequency domain plots of a 3 Hz signal

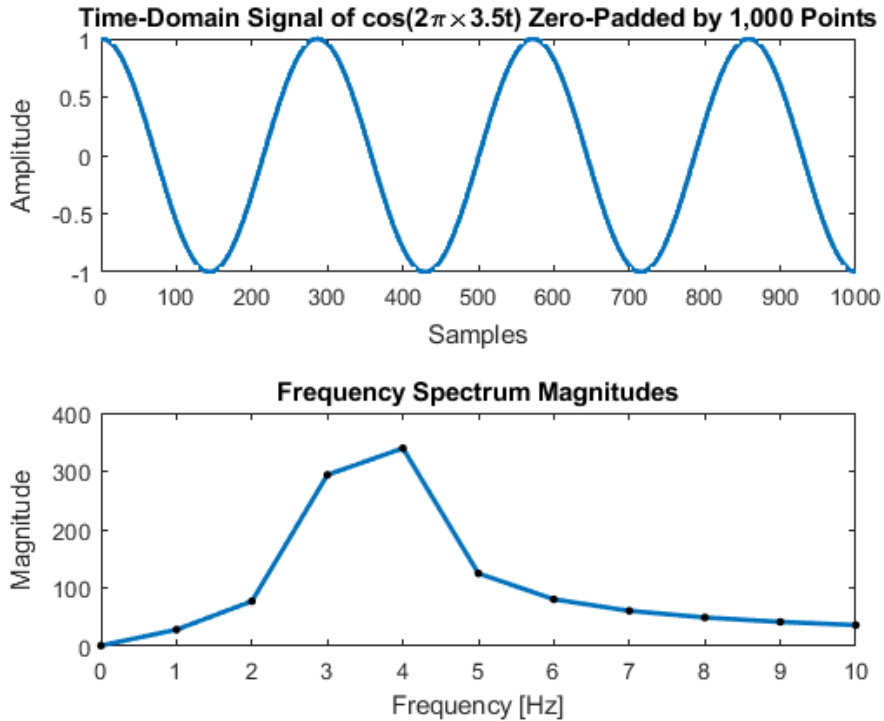


Figure 18. Time and frequency domain plots of a 3.5 Hz signal

“Zero padding” is a method used to find the correct signal frequencies and their magnitudes. This does not enhance the frequency resolution of the signal but rather decreases the size of the frequency bins. The resolution of the signal can only be refined by lengthening the sample window. The signal is artificially lengthened by adding a series of zeros at the end of the signal’s time domain. Figure 19 shows the same 3.5 Hz signal, but it is zero-padded by 1,000 points. A closer look at the frequency spectrum shows that adding 1,000 DFT points resolved the 3.5 Hz frequency at the expected magnitude since the bin size of the signal is now 0.5 Hz. The length of the signal is usually zero-padded to any exponential of two ( $2^n$ ) so that fast Fourier transform (FFT) algorithms can quickly calculate the DFT of the signal. However, a consequence of zero-padding is the introduction of side lobes that distort the frequency spectrum. If multiple frequencies are present in a signal, the magnitudes of other frequencies may be

affected by the side lobes. Increasing the number of DFT points does not actually resolve this issue. Instead, as illustrated in Figure 20, the density of the DFT samples increases.

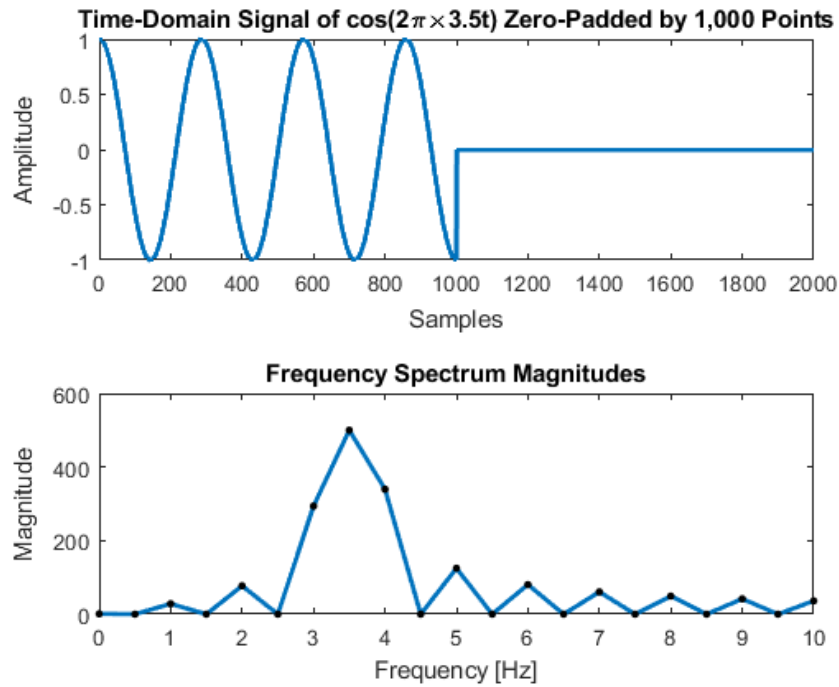


Figure 19. Time and frequency domain plots of a 3.5 Hz signal zero-padded by 1,000 points

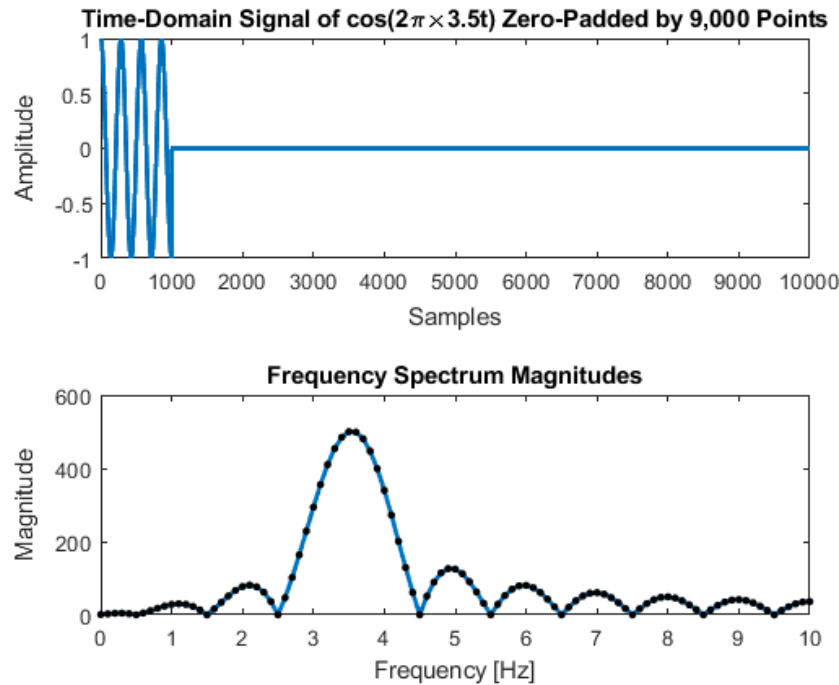


Figure 20. Time and frequency domain plots of a 3.5 Hz signal zero-padded by 9,000 points

### 3.2.2 Windowing the Vibration Data

Since FFT algorithms repeat the signal infinitely in time, unwanted noise could occur as a consequence of discontinuities in the time domain. An approach to minimize noise caused by “zero padding” is to implement a time-domain windowing function on the original signal. Most window functions essentially have both endpoints of the original time-domain signal gradually approach zero and allows the waveform to repeat infinitely with no discontinuities. Hanning window functions are typically used for vibration data as it minimizes the side lobe peaks while maintaining a good frequency resolution [23]. Figure 21 demonstrates the Hanning window applied to a 3.5 Hz signal zero-padded by 9,000 points. The frequency spectrum plot clearly shows that the side lobe peaks were significantly reduced. However, the width of the main lobe doubled, which distorts adjacent frequency bins but maintains the expected magnitude of the 3.5 Hz signal.

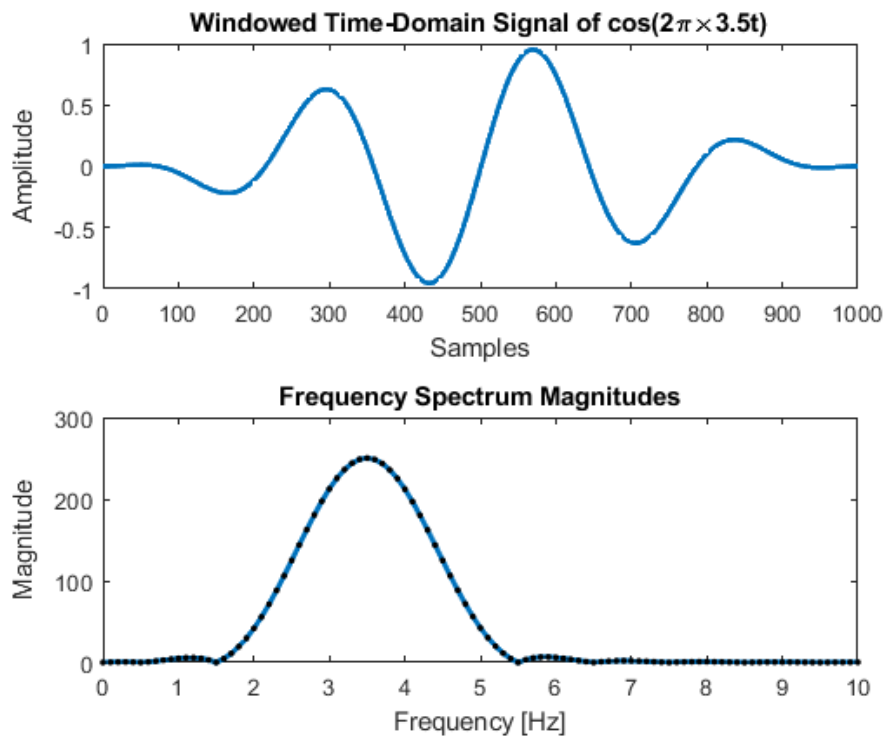


Figure 21. Hanning window function applied to a 3.5 Hz signal zero-padded by 9,000 points

### 3.2.3 Normalized Defect Energy and the Hunting/Integration Ranges

Depending on the frequency bin resolution chosen and the effects of windowing, the hunting and integration ranges that were discussed in Section 3.1.2 would have to be optimized to find the correct fundamental defect frequencies and normalized defect energies. If the identification of the correct defect type remains inaccurate after optimizing the hunting and integration ranges, alternative calculations of the normalized defect energies would have to be devised. Montalvo [19] developed an alternative method that enhances the *certainty* of the detected defect type by squaring the normalized defect energies. This approach amplifies the highest normalized defect energy percentage that might be slightly below the 50% threshold to a percentage that meets the 50% criterion of Eq. (13). However, a drawback of this method is that it can also inflate the NDE percentages of incorrectly identified defect types by the defect detection algorithm. Having said that, the reliability of the developed defect detection algorithm has been tested extensively through laboratory and field testing and has been found to be predominantly accurate. Hence, it is prudent that higher exponentials of the normalized defect energies be considered as a way to enhance the certainty of the defect detection.

## CHAPTER IV

### RESULTS AND DISCUSSION

The effectiveness of the wireless module and the optimizations done for the defect detection algorithm are discussed in this chapter. Several laboratory experiments were conducted to validate the first two levels of the defect detection algorithm for the wireless module by directly comparing its results to a wired accelerometer on the outboard smart adapter location (refer to Figure 10). The defect types and their locations for each experiment are given in Table 2. To represent one value for each speed and load combination, the mean RMS vibration values and normalized defect energy (NDE) values were calculated for Level 1 and Level 2 analyses, respectively. Values from the Level 1 and Level 2 analyses for all experiments will be summarized in tables. RMS vibration values greater than the preliminary threshold ( $T_p$ ) from the Level 1 tables will be *italicized*, while RMS vibration values greater than the maximum threshold ( $T_{max}$ ) in the Level 1 tables and percentages of the NDE values above 50% from the Level 2 tables will be **bolded**.

It is important to note that Level 3 analysis of the algorithm will not be optimized in this study since this step is based on a correlation between the vibration RMS values and their corresponding defect areas, which has already been optimized by Lima [22].

Table 2. Corresponding defect type for each experiment

Experiment No.	Defect Type and Location	Defect Area [cm <sup>2</sup> ]/[in <sup>2</sup> ]
221	Inboard (IB) Cup	3.76/0.58
224	Outboard (OB) Cone	10.84/1.68
228	Inboard (IB) Cone	15.4/2.39
228B	Outboard (OB) Cone	16.19/2.51
232	Outboard (OB) Cup	20.1/3.12

#### 4.1 Level 1: Is the Bearing Defective?

The main objective of this analysis step is to verify whether the wireless module can accurately and reliably determine the bearing condition. The performance of the wireless module will be assessed by comparing it to the performance of the wired module. Table 3 and Table 4 compare the average vibration RMS values for both the wireless and wired sensor modules at the unloaded and loaded railcar conditions, respectively. The results show that the vibration RMS values for the wireless module are very comparable to those of the wired module as they are both within  $\pm 1g$  for most test conditions listed in Table 3 and Table 4. Both wireless and wired devices indicate that there are possible defects in the bearings of Experiments 228 and 228B since their RMS values are above the  $T_p$ , whereas, the bearings in Experiments 221, 224, and 232 are found to be definitely defective as their RMS values are above the  $T_{max}$ . These RMS values will prompt the algorithm to move onto Level 2 analysis.

Table 3. Average vibration RMS values at 17% load

17% Load (simulating empty railcar)						
Exp	RPM	420	467	498	560	618
221 (IB Cup)	Wireless RMS [g]	<b>4.2</b>	-	<b>6.1</b>	<b>7.0</b>	-
	Wired RMS [g]	3.9	-	<b>5.2</b>	<b>7.3</b>	-
224 (OB Cone)	Wireless RMS [g]	-	-	2.9	<b>7.8</b>	<b>7.1</b>
	Wired RMS [g]	-	-	<b>8.1</b>	<b>7.9</b>	<b>11.5</b>
228 (IB Cone)	Wireless RMS [g]	-	3.2	3.7	-	5.1
	Wired RMS [g]	-	4.2	4.5	-	5.2
228B (OB Cone)	Wireless RMS [g]	-	-	2.7	3.7	3.5
	Wired RMS [g]	-	-	3.2	4.2	3.8
232 (OB Cup)	Wireless RMS [g]	<b>7.0</b>	-	<b>8.0</b>	<b>8.7</b>	-
	Wired RMS [g]	<b>7.5</b>	-	<b>9.2</b>	<b>11.8</b>	-
$T_p$ [g]		2.0	2.2	2.3	2.6	2.9
$T_{max}$ [g]		4.0	4.5	4.9	5.7	6.3

Table 4. Average vibration RMS values at 100% load

100% Load (simulating a full railcar)						
Exp	RPM	420	467	498	560	618
221 (IB Cup)	Wireless RMS [g]	-	-	4.5	4.4	-
	Wired RMS [g]	-	-	3.2	4.0	-
224 (OB Cone)	Wireless RMS [g]	-	-	-	<b>7.4</b>	<b>7.2</b>
	Wired RMS [g]	-	-	-	<b>10.2</b>	<b>10.1</b>
228 (IB Cone)	Wireless RMS [g]	-	4.2	4.8	-	5.1
	Wired RMS [g]	-	3.7	3.8	-	5.2
228B (OB Cone)	Wireless RMS [g]	-	3.7	4.2	5.6	5.8
	Wired RMS [g]	-	3.3	3.4	4.7	5.0
232 (OB Cup)	Wireless RMS [g]	<b>11.3</b>	-	<b>13.9</b>	<b>17.1</b>	-
	Wired RMS [g]	<b>9.3</b>	-	<b>14.7</b>	<b>13.5</b>	-
$T_p$ [g]		2.0	2.2	2.3	2.6	2.9
$T_{max}$ [g]		4.0	4.5	4.9	5.7	6.3

## 4.2 Level 2: What is the Defect Type?

### 4.2.1 Zero padding the vibration data

Before comparing the Level 2 analysis for both wireless and wired devices, the effectiveness of the original algorithm for the wireless module must be optimized. The original



algorithm has the vibration data zero-padded to the next exponential of two. Since the wireless module collects 5,200 samples, the vibration data would be zero-padded to 8,192 samples, and the NDE values (given as “max/sum” percentage) are calculated from the generated power spectral density (PSD) plots. However, as demonstrated in Table 5, applying the original algorithm on the wireless sensor module data yields inaccurate results in identifying the correct defect type and low *certainty* (as measured by the NDE “max/sum” percentage) in the identified defect. To improve the reliability of the defect identification and defect certainty, zero padding the vibration data to higher exponentials of two ( $2^n$ ) was also analyzed. The NDEs calculated for each case of zero-padding are summarized in Table 5. Examining the results, it is apparent that zero padding to 65,536 points gives the best results in identifying the correct defect type and defect certainty, but more computational power is required to analyze the large number of data points. Using the MATLAB™ profiler, Figure 22 displays the time periods the algorithm ran for each zero-padding case, which is calculated by subtracting the “Self Time” from the “Total Time.” Looking at the data of Figure 22, there is a significant increase in computation time when zero padding to 65,536 points, and the results are not that much better from zero padding to 32,768 points, which ultimately eliminates it as a possible optimization option. Similarly, zero padding to 32,768 points does not improve the results significantly when compared with zero padding to 16,384 points, and the difference in computation time between these two cases is negligible. Nevertheless, the identification of the correct defect type and defect certainty are still fairly low when zero padding to either 16,384 or 32,768 points. Hence, other optimizations in the algorithm must be implemented to justify whether the vibration data should be zero-padded to 16,384 or 32,768 points.

Table 5. Effectiveness of zero-padding on defect identification and its certainty

Zero Padding Analysis	Experiment No.	Correct Defect Type Identified [%]	Max/Sum [%]
Zero-Padded to 8,192 Points	221	77	45
	224	60	36
	228	67	51
	228B	57	35
	232	100	49
Zero-Padded to 16,384 Points	221	85	49
	224	100	38
	228	63	35
	228B	65	36
	232	100	51
Zero-Padded to 32,768 Points	221	92	57
	224	100	37
	228	59	36
	228B	71	36
	232	100	59
Zero-Padded to 65,536 Points	221	100	62
	224	100	37
	228	63	36
	228B	57	36
	232	100	63

	Function Name	Calls	Total Time	Self Time*	Total Time Plot (dark band = self time)
65,536 Points	<a href="#">WirelessModule_ThresholdRMS_Time</a>	1	6.881 s	1.745 s	
32,768 Points	<a href="#">WirelessModule_ThresholdRMS_Time</a>	1	5.087 s	1.137 s	
16,384 Points	<a href="#">WirelessModule_ThresholdRMS_Time</a>	1	4.625 s	0.876 s	
8,192 Points	<a href="#">WirelessModule_ThresholdRMS_Time</a>	1	4.446 s	0.747 s	

Figure 22. Algorithm speed for various zero-padding cases

#### 4.2.2 Applying a Hanning window function to the vibration data

To determine if the frequency spectrum is significantly distorted by the side lobes created from zero-padding, a Hanning window function that was discussed in Section 3.2.2 is applied to the vibration data. Table 6 summarizes the effects of applying a Hanning window on Level 2

analysis results. It turns out that applying a Hanning window did not improve the identification of the correct defect type and defect certainty. In fact, one can argue that the results are slightly worse. This conclusion proves that the magnitudes from the harmonics of the fundamental defect frequencies are not distorted by the side lobes that result from zero-padding the wireless sensor data.

Table 6. Effect of using a Hanning window function on defect identification and its certainty

Windowing Analysis	Experiment No.	Correct Defect Type Identified [%]	Max/Sum [%]
<b>Hanning Window &amp; Zero-Padded to 16,384 Points</b>	221	76	50
	224	91	37
	228	59	35
	228B	63	36
	232	100	56
<b>Hanning Window &amp; Zero-Padded to 32,768 Points</b>	221	76	51
	224	90	40
	228	50	36
	228B	64	36
	232	100	60

#### 4.2.3 Modifying the hunting and integration ranges

Since applying a Hanning window function did not improve the Level 2 analysis results, the next step was to optimize the hunting and integration ranges. The ideal “Hunting Factor” which would be multiplied by the frequency-bin resolution ( $r_s$ ) to obtain the hunting range ( $h_r$ ) was first explored. The integration range ( $i_r$ ) was set to equal the frequency-bin resolution for this analysis. The NDEs were then calculated for the different hunting ranges ( $h_r$ ) examined and used to identify the defect type.

Table 7 and Table 8 summarize the results obtained for the different hunting factors explored for 16,384 points and 32,768 points, respectively, at medium (350 – 610 RPM) and high speeds (> 610 RPM). The hunting factors that produced the best percentages of identifying

the correct defect type for medium and high speeds are highlighted in yellow. Comparing the results of Table 7 and Table 8, at first glance, it appears that zero-padding to 32,768 points gives a slightly higher chance of the algorithm identifying the correct defect type at the medium speeds (350 – 610 RPM) as compared to zero-padding to 16,384 data points. However, zero-padding to 32,768 points requires significantly higher hunting factors to achieve slightly better results. If one compares the results of Table 7 and Table 8 for a hunting factor of 8, then zero-padding to 16,384 data points clearly gives the better percentages for identifying the correct defect type.

Table 7. Finding the optimal hunting ranges for zero-padding to 16,384 data points

	Hunting Factor	Correct Defect Type Identified [%]					AVG
		221	224	228	228B	232	
<b>350 - 610 RPM</b> $i_r = rS$ $= \pm 0.3174 \text{ Hz}$	1	94	100	39	50	75	71.6
	2	100	67	54	60	83	72.9
	3	100	67	49	66	92	74.8
	4	100	33	53	59	100	69.0
	5	88	67	53	74	100	76.3
	6	94	100	60	71	100	84.9
	7	94	67	55	78	100	78.8
	8	94	100	56	76	100	85.4
	9	94	67	59	79	100	79.8
	10	94	67	64	79	100	80.7
	11	94	67	66	79	100	81.3
	12	88	67	66	79	100	80.1
	13	88	67	67	79	100	80.3
	14	82	67	63	79	100	78.3
	15	82	67	62	76	100	77.5
	16	76	67	62	75	100	76.0
	17	71	67	64	76	100	75.6
	18	82	67	65	78	100	78.4
	19	82	67	67	71	100	77.4
	20	76	67	70	79	100	78.4
<b>&gt; 610 RPM</b> $i_r = rS$ $= \pm 0.3174 \text{ Hz}$	1	-	38	18	50	-	35.2
	2	-	63	55	38	-	51.5
	3	-	88	50	50	-	62.5
	4	-	63	55	75	-	64.0
	5	-	75	77	63	-	71.6
	6	-	88	73	50	-	70.1
	7	-	88	59	100	-	82.2
	8	-	100	68	88	-	85.2
	9	-	100	59	75	-	78.0
	10	-	100	64	63	-	75.4
	11	-	100	64	75	-	79.5
	12	-	100	59	88	-	82.2
	13	-	100	64	88	-	83.7
	14	-	100	67	88	-	84.8
	15	-	100	67	88	-	84.8
	16	-	100	64	75	-	79.5
	17	-	100	64	63	-	75.4
	18	-	100	59	63	-	73.9
	19	-	100	55	75	-	76.5
	20	-	100	55	75	-	76.5

Table 8. Finding the optimal hunting ranges for zero-padding to 32,768 data points

	Hunting Factor	Correct Defect Type Identified [%]					AVG
		221	224	228	228B	232	
<b>350 - 610 RPM</b> $i_r = rS$ $= \pm 0.1587 \text{ Hz}$	1	88	33	42	34	75	54.5
	2	94	100	39	47	92	74.3
	3	94	100	58	65	92	81.6
	4	94	0	69	62	92	63.4
	5	94	67	61	66	92	76.0
	6	100	67	56	66	100	77.9
	7	100	33	59	66	100	71.7
	8	94	100	56	68	100	83.6
	9	100	100	56	72	100	85.7
	10	82	100	59	71	100	82.4
	11	88	100	61	69	100	83.6
	12	88	67	58	74	100	77.4
	13	88	67	63	71	100	77.7
	14	88	67	64	81	100	80.0
	15	94	67	67	75	100	80.6
	16	94	67	70	78	100	81.7
	17	94	100	66	81	100	88.3
	18	94	67	71	82	100	82.8
	19	94	100	71	82	100	89.5
	20	94	100	71	78	100	88.6
<b>&gt; 610 RPM</b> $i_r = rS$ $= \pm 0.1587 \text{ Hz}$	1	-	13	14	38	-	21.2
	2	-	50	18	50	-	39.4
	3	-	50	32	50	-	43.9
	4	-	88	45	25	-	52.7
	5	-	88	45	38	-	56.8
	6	-	100	45	50	-	65.2
	7	-	100	64	50	-	71.2
	8	-	88	59	50	-	65.5
	9	-	100	68	50	-	72.7
	10	-	63	64	63	-	62.9
	11	-	100	68	75	-	81.1
	12	-	100	50	75	-	75.0
	13	-	100	68	88	-	85.2
	14	-	100	59	88	-	82.2
	15	-	100	64	88	-	83.7
	16	-	88	59	88	-	78.0
	17	-	88	55	88	-	76.5
	18	-	88	50	88	-	75.0
	19	-	100	59	88	-	82.2
	20	-	100	64	88	-	83.7

Now that the optimal hunting ranges for both zero-padding cases have been identified, a similar process was followed to determine the ideal “Integration Factor” for both zero-padding cases. These results are presented in Table 9 and Table 10. The “Integration Factor” is multiplied by the frequency-bin resolution to get the integration range ( $i_r$ ). The results clearly show that increasing the integration factor beyond “1” does not improve the identification of the correct defect type. This is likely due to the fact that the normalized defect energies (NDEs) calculated using larger integration ranges capture some of the vibration energy from other neighboring frequencies, which negatively affects the accuracy of the calculations.

Table 9. Finding the optimal integration ranges for zero-padding to 16,384 data points

	Integration Factor	Correct Defect Type Identified [%]					AVG
		221	224	228	228B	232	
<b>350 - 610 RPM</b> $h_r = r_s \times 8$ $= \pm 2.54 \text{ Hz}$	1	94	100	56	76	100	85.4
	2	94	100	53	79	100	85.3
	3	94	100	51	78	100	84.5
	4	94	100	47	71	100	82.4
	5	94	67	49	71	100	76.2
<b>&gt; 610 RPM</b> $h_r = r_s \times 8$ $= \pm 2.54 \text{ Hz}$	Correct Defect Type Identified [%]						AVG
	1	-	100	68	88	-	85.2
	2	-	100	59	88	-	85.2
	3	-	100	36	63	-	66.3
	4	-	88	27	75	-	63.3
	5	-	88	23	88	-	65.9

Table 10. Finding the optimal integration ranges for zero-padding to 32,768 data points

	Integration Factor	Correct Defect Type Identified [%]					AVG
		221	224	228	228B	232	
<b>350 - 610 RPM</b> $h_r = r_s \times 19$ $= \pm 3.02 \text{ Hz}$	1	94	100	71	82	100	89.5
	2	94	100	71	82	100	89.4
	3	94	100	70	82	100	89.2
	4	94	100	68	81	100	88.6
	5	94	100	67	80	100	88.2
<b>&gt; 610 RPM</b> $h_r = r_s \times 13$ $= \pm 2.06 \text{ Hz}$	Correct Defect Type Identified [%]						AVG
	1	-	100	68	88	-	85.2
	2	-	100	68	88	-	85.2
	3	-	100	68	88	-	85.2
	4	-	100	68	88	-	85.2
	5	-	100	68	88	-	85.2

Table 11 presents the improvements made by modifying the hunting and integration ranges for both zero-padding cases. The results indicate that the identification of the correct defect type has improved slightly, but the underlying issue of obtaining better certainties in the identification of the defect type remains. Furthermore, the results also demonstrate that the accuracy and reliability of identifying cup (outer ring) defects is better than that for cone (inner ring) defects. The latter is not surprising since cups are stationary while cones rotate in and out of the loaded zone making it slightly harder to identify defects on their raceways.



Table 11. Summary of the optimal hunting/integration ranges

Hunt/Int Ranges	Experiment No.	Correct Defect Type Identified [%]	Max/Sum [%]
<b>Zero-Padded to 16,384 Points and Modified <math>h_r / i_r</math></b>	221	94	52
	224	100	38
	228	59	36
	228B	78	37
	232	100	60
<b>Zero-Padded to 32,768 Points and Modified <math>h_r / i_r</math></b>	221	94	55
	224	100	37
	228	70	36
	228B	85	37
	232	100	57

To further illustrate the previous findings, the power spectral density (PSD) plot of Experiment 228, which has a cone defect on the inboard side of the bearing, is plotted in Figure 23. This plot shows that there are no substantial peaks that occur at the cone defect fundamental frequency and its harmonics as compared to the other two defect frequencies. This phenomenon can be explained by the following two factors. First, unlike the wired sensor module which is equipped with a 16<sup>th</sup> order filter to eliminate high frequency noise, to minimize power consumption, the wireless module architecture does not support a noise filter. That coupled with the fact that the wireless sensor only collects a one-second sample window, introduces noise throughout the spectrum, which makes it difficult to determine the correct fundamental defect frequencies using the selected hunting ranges. Second, the cone defect in this particular experiment was located in the inboard side of the bearing, whereas the wireless sensor module was affixed to the outboard side of the bearing. This arrangement can result in the magnitudes of the cone defect frequencies to be much smaller than they would be had the cone defect were on the outboard side of the bearing. This is supported by the fact that the percentages of the correct defect type identification are significantly higher for the other two cone defects which were

located on the outboard side of the bearing (i.e., same side as wireless sensor module location). Additional evidence supporting these findings is the inability of the Trackside Acoustic Detector Systems (TADS) to identify inboard cone defects. On a positive note, the proposed algorithm studied here can correctly identify inboard cone defects albeit with a slightly lower certainty than in the case of outboard cone defects. Given the nature of the frequency spectrum shown in Figure 23, further optimization of the hunting and integration ranges will not yield better results.

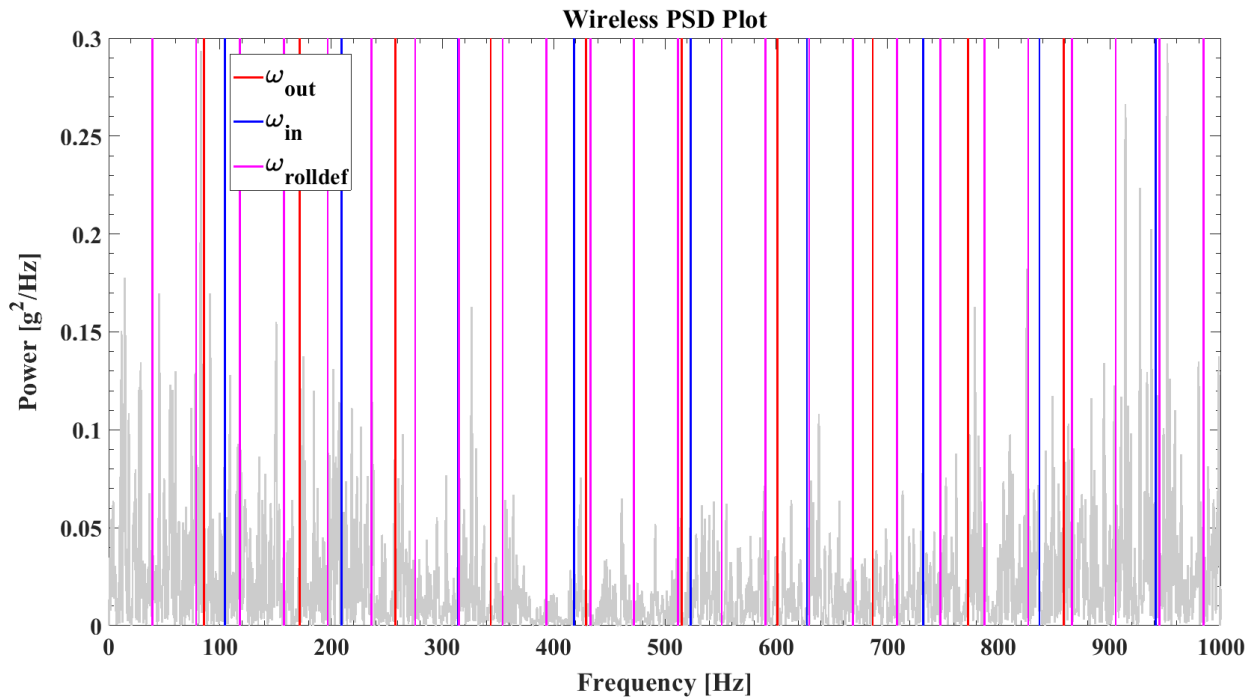


Figure 23. A PSD plot of Experiment 228 with the fundamental defect frequencies and their harmonics shown

Since it is still not clear which zero-padding case gives the best results while also optimizing power consumption, both cases (i.e., zero-padding to 16,384 and 32,768 points) will still be analyzed for further optimizations of the algorithm.

#### 4.2.4 Modifying the normalized defect energy (NDE) calculations

To further improve the identification of the correct defect type and the defect certainty, modifications to the NDE calculations were explored. Normally, to find the NDE, the algorithm sums up all the areas under the defect frequency and its harmonics in a 1,000 Hz frequency range and divides that by the total number of harmonics within that frequency range. However, referring back to Figure 13, each type of defect frequency has a different number of harmonics in the 1,000 Hz frequency range in. So, instead of averaging the areas for *all* harmonics of a defect frequency in a 1,000 Hz frequency range, each defect type would only average the areas for the *same number* of harmonics. Table 12 and Table 13 summarize the analysis carried out to find the best identification percentage of the correct defect type for 16,384 and 32,768 data points, respectively. Calculating the NDEs up to the ninth harmonic using Eqs. (14) – (16) gave the best identification percentage of the correct defect type when zero-padding to 16,384 data points. However, in the case of zero-padding to 32,768 data point, the best percentages were achieved when the NDEs were calculated up to the sixth harmonic, albeit with slightly lower correct identification percentages in the cases of Experiment 228 and 228B.

Table 12. Optimizing the normalized defect energy calculations for 16,384 data points

	Harmonic	Correct Defect Type Identified [%]					AVG
		221	224	228	228B	232	
All Experiments (16,384 Points)	1	29	91	79	84	92	75.1
	2	88	91	81	89	100	89.9
	3	88	91	86	91	100	91.3
	4	88	91	86	92	100	91.5
	5	82	100	89	91	100	92.5
	6	82	100	87	93	100	92.6
	7	82	100	86	93	100	92.3
	8	82	100	87	95	92	91.2
	9	88	100	92	99	100	95.8
	10	76	100	93	97	100	93.3
	11	71	100	86	96	100	90.6
	12	71	100	86	96	100	90.6
	13	82	100	87	96	100	93.2
	14	88	100	87	96	83	91.0
	15	88	100	87	96	83	91.0

Table 13. Optimizing the normalized defect energy calculations for 32,768 data points

	Harmonic	Correct Defect Type Identified [%]					AVG
		221	224	228	228B	232	
All Experiments (32,768 Points)	1	35	91	78	86	92	76.4
	2	82	91	82	91	100	89.2
	3	88	91	85	92	100	91.2
	4	88	91	85	95	100	91.7
	5	88	100	87	92	100	93.5
	6	88	100	87	95	100	94.1
	7	88	100	86	95	100	93.7
	8	76	100	88	96	100	92.2
	9	76	100	93	97	100	93.3
	10	76	100	93	99	100	93.6
	11	76	100	91	99	100	93.2
	12	76	91	91	97	100	91.1
	13	76	91	91	97	92	89.5
	14	71	91	92	97	83	86.8
	15	71	91	91	97	83	86.6

$$NDE_{cup} = \frac{\sum_{i=1}^9 \int_{i\omega_{out}-i_r}^{i\omega_{out}+i_r} |X(f)|^2 df}{9} \quad (14)$$

$$NDE_{cone} = \frac{\sum_{i=1}^9 \int_{i\omega_{in}-i_r}^{i\omega_{in}+i_r} |X(f)|^2 df}{9} \quad (15)$$

$$NDE_{roller} = \frac{\sum_{i=1}^9 \int_{i\omega_{rolldef}-i_r}^{i\omega_{rolldef}+i_r} |X(f)|^2 df}{9} \quad (16)$$

Now that the identification of the correct defect type has been optimized for use with the wireless sensor module that collects one-second sample data, attention is turned to optimizing the defect certainty percentages. To that end, Table 14 summarizes the results of the optimal normalized defect energy calculations, where the cells highlighted in yellow indicate the corresponding defect type for each experiment.

Table 14. Summary of the optimal normalized defect energy calculations

Normalized Defect Energy (NDE)	Experiment No.	Correct Defect Type Identified [%]	Average Cup Defect Certainty [%]	Average Cone Defect Certainty [%]	Average Roller Defect Certainty [%]
<b>Zero-Padded to 16,384 Points, Modified <math>h_r / i_r</math>, and Modified NDE Calculation</b>	221	88	53	35	12
	224	100	29	56	15
	228	92	36	45	19
	228B	99	36	47	17
	232	100	59	32	9
<b>Normalized Defect Energies Squared</b>	221	88	64	32	4
	224	100	21	74	5
	228	92	36	53	11
	228B	99	33	58	9
	232	100	72	26	2
<b>Normalized Defect Energies Cubed</b>	221	88	69	30	1
	224	100	15	83	2
	228	92	33	60	7
	228B	99	30	66	4
	232	100	78	21	1

Examining Table 14, it can be seen that modifying the NDE calculations, as shown earlier, significantly improved both the identification of the correct defect type and the defect certainty in each experiment. Furthermore, the percent certainty of the correct defect type is shown to be greater than the percent certainties of the other defect types. However, Experiments 228 and 228B have the percent certainty of the cone defect barely miss the 50% threshold. This can be visually unappealing to a user viewing this analysis since percentages below 50% can be perceived negatively even though they identify the correct defect type present in the bearing. To remedy this situation, the normalized defect energy squared method, that was discussed in Section 3.2.3, was applied. Table 14 shows that this approach enhanced the defect certainties that were slightly lower than 50% to percentages that meet the 50% criterion while also providing further distinction from the certainty percentages of the other two defect types. The optics of this analysis can be further improved by cubing the normalized defect energies. Having higher percent certainty of the identified defect type allows the end user to be more confident with the results obtained from the Level 2 analysis.

It is worth mentioning at this point that squaring or cubing the NDEs to improve the optics of the defect certainties is not without any consequences as incorrectly identified defect types will also have their certainties boosted giving false positives. However, this is not a great concern since false positives are very uncommon when utilizing this optimized algorithm, and the few cases that occur are restricted to operating conditions where the railcars are empty (unloaded). To support the latter conclusions, a summary of Level 2 analysis for unloaded and loaded railcar conditions using the optimized algorithm described here is given in Table 15 and Table 16, respectively. Examining the results of Table 15 and Table 16, one can clearly see that false positives, as gauged by the percentages of correctly identified defect types, are not a major

concern and only occur when the railcar is unloaded (i.e., an empty railcar). This finding is relevant since bearing defects do not usually propagate when the railcars are unloaded [24].

Looking at Table 15 and Table 16, more observations can be made about the accuracy and reliability of the wireless sensor module. In general, the defect certainties tend to improve as the speed increases, and loading conditions have a more pronounced effect on the defect certainty than speed. Moreover, defects on the outboard side of the bearing (i.e., same side as sensor module location) have much better defect certainties than inboard side defects. The percent certainties of the defects on the inboard side of the bearing are higher under full railcar load conditions. Finally, the results show that the accuracy and reliability of detecting cup load conditions. Finally, the results show that the accuracy and reliability of detecting cup defects are higher than those of detecting cone defects, as was explained earlier in this chapter.

Table 15. Level 2 analysis for 17% load (empty railcar) using the optimized algorithm

<b>17% Load (simulating an empty railcar)</b>						
<i>Experiment No.</i>	<i>Sensor Module Type</i>	<i>Max/Sum [%] for Different RPM</i>				
		<i>420</i>	<i>467</i>	<i>498</i>	<i>560</i>	<i>618</i>
221 (IB Cup)	<i>Wireless</i>	<b>58</b>	-	<b>59</b>	<b>54</b>	-
	<i>Wired</i>	<b>99</b>	-	<b>98</b>	<b>100</b>	-
224 (OB Cone)	<i>Wireless</i>	-	-	<b>99</b>	<b>76</b>	<b>88</b>
	<i>Wired</i>	-	-	<b>75</b>	<b>96</b>	<b>99</b>
228 (IB Cone)	<i>Wireless</i>	-	<b>58</b>	<b>63</b>	-	<b>58</b>
	<i>Wired</i>	-	<b>92</b>	<b>96</b>	-	<b>86</b>
228B (OB Cone)	<i>Wireless</i>	-	-	<b>65</b>	<b>63</b>	<b>75</b>
	<i>Wired</i>	-	-	<b>88</b>	<b>88</b>	<b>96</b>
232 (OB Cup)	<i>Wireless</i>	<b>69</b>	-	<b>87</b>	<b>100</b>	-
	<i>Wired</i>	<b>100</b>	-	<b>100</b>	<b>100</b>	-
<b>Correct Defect Type Identified [%]</b>						
<i>Wireless</i>		100	75	88	95	95
<i>Wired</i>		100	100	100	100	100

Table 16. Level 2 analysis for 100% load (full railcar) using the optimized algorithm

17% Load (simulating a full railcar)						
Experiment No.	Sensor Module Type	Max/Sum [%] for Different RPM				
		420	467	498	560	618
221 (IB Cup)	Wireless	-	-	<b>74</b>	<b>98</b>	-
	Wired	-	-	<b>99</b>	<b>100</b>	-
224 (OB Cone)	Wireless	-	-	-	<b>67</b>	<b>82</b>
	Wired	-	-	-	<b>99</b>	<b>99</b>
228 (IB Cone)	Wireless	-	<b>64</b>	<b>65</b>	-	-
	Wired	-	<b>92</b>	<b>96</b>	-	-
228B (OB Cone)	Wireless	-	<b>74</b>	<b>67</b>	<b>66</b>	<b>72</b>
	Wired	-	<b>91</b>	<b>90</b>	<b>96</b>	<b>98</b>
232 (OB Cup)	Wireless	<b>59</b>	-	<b>70</b>	<b>62</b>	-
	Wired	<b>90</b>	-	<b>99</b>	<b>99</b>	-
Correct Defect Type Identified [%]						
Wireless		100	100	100	100	100
Wired		100	100	100	100	100

While the Level 2 analysis for the wireless sensor module did not attain the same level of accuracy and reliability as that for the wired sensor module, the optimized algorithm described here still produces reliable and accurate assessments of bearing health and correct identification of the defect type in the case of defective bearings. More importantly, the optimized algorithm for use with the wireless sensor module only uses one-second sample windows to perform the bearing health assessment while expending significantly less computation power than its wired counterpart. Using the MATLAB™ profiler, Figure 24 demonstrates that the optimized algorithm is more than five times faster than the original algorithm used with the wired sensor module.


Function Name	Calls	Total Time	Self Time*	Total Time Plot (dark band = self time)
<a href="#">WiredADXL_Time</a>	1	21.190 s	1.970 s	
<a href="#">WirelessModule_ThresholdRMS_Time</a>	1	4.538 s	0.925 s	

Figure 24. Algorithm speed comparing the wired accelerometer and the wireless module



Finally, identifying the correct defect type will prompt the algorithm to proceed to Level 3 analysis. However, this step of the algorithm will not be analyzed here as the vibration RMS values of the wireless sensor module are very comparable to those of the wired sensor module, and thus, similar results will be obtained since Level 3 analysis depends on a correlation that relates the RMS values of the sensors to the defect size. Readers are referred to the thesis by Montalvo [19] which demonstrates the use of Level 3 analysis to acquire estimates of the defect size within bearings.

#### **4.2.5 Validation of the optimized algorithm for roller defects**

Since a bearing containing roller defects was not tested with the wireless sensor module, the optimized algorithm was tested on a previously performed experiment in which a wired sensor module was used to monitor a bearing that contained three defective rollers on the outboard side cone assembly. Table 17 provides a direct comparison between the Level 2 analysis of the original algorithm that uses a four-second sample window and the Level 2 analysis done with the optimized algorithm that uses a one-second sample window. Both algorithms correctly identify the defect type with percent certainties that are substantially greater than the 50% threshold criterion, which validates the functionality of the optimized algorithm in detecting bearings with roller defects. The lower percent certainty of the optimized algorithm is expected since it only uses a one-second sample window for the analysis, whereas the original algorithm uses four-second sample windows, which helps enhance the percent certainty of the defect detection.

Table 17. Algorithm comparison of Level 2 analysis for a bearing containing roller defects

<b>100% Load (simulating a full railcar) and an RPM of 560 (simulating 106 km/h or 60 mph)</b>			
<i>Experiment No.</i>	<i>Algorithm Used</i>	<i>Max/Sum [%]</i>	<i>Defect Type</i>
078A (OB Roller x3)	<i>Original (4 seconds of vibration data)</i>	<b>89</b>	<b>Roller</b>
	<i>Optimized (1 second of vibration data)</i>	<b>67</b>	<b>Roller</b>

## CHAPTER V

### CONCLUSIONS

A wireless onboard condition monitoring module utilizing one-second sample windows of vibration data collected at a rate of 5200 Hz to assess the bearing health was designed and fabricated. The efficacy of this wireless module in accurately and reliably assessing the bearing health was validated against the performance of a wired module that uses four-second sample windows to analyze the bearing condition. The wired module was used as the reference since it has been in use for more than half a decade now and has been proven through several studies to be accurate and reliable in assessing the health of bearings.

Bearings containing a defective inner ring (cone) or outer ring (cup) of various defect sizes (areas) were tested on a dynamic single bearing test rig (SBT). Several methods were explored to optimize the original bearing defect detection algorithm, developed by Montalvo [19], for the wireless sensor module to attain accurate assessments of the bearing condition while minimizing the computation power consumption. Level 3 analysis, which is based on an experimentally formulated correlation between vibration RMS values and their corresponding defect areas, was not explored in this study since it has already been optimized by Lima [22].

The results from this study demonstrate that the wireless sensor module can accurately assess the bearing health (Level 1 analysis) using only one second of vibration data recorded at a sampling rate of 5200 Hz. The results of this study demonstrate that the RMS vibration values collected by the wireless module are comparable to those recorded by the wired module for the

same bearing operated at the same load and speed conditions. The results also indicated that there was no need to make any changes to the previously developed preliminary threshold ( $T_p$ ) and maximum threshold ( $T_{max}$ ). So, RMS vibration values that are above the  $T_p$  indicate a possible defect within the bearing, while RMS values above the  $T_{max}$  imply that the bearing is defective. Once the RMS vibration values are found to be above the  $T_p$  or the  $T_{max}$ , the power spectral density (PSD) plots are generated for the purpose of identifying the defective component (Level 2 analysis) by calculating the normalized defect energy (NDE) values for the cup, cone, and roller defects. In the original algorithm, ratios of the maximum NDE divided by the sum of all three NDEs that were over the 50% criterion would classify the component with the highest NDE value to have a localized defect (i.e., cup, cone, or roller). However, Level 2 analysis of the original algorithm was found to be inefficient in identifying the correct defect type when implemented with the newly designed and fabricated wireless sensor module. So, several optimizations had to be made to the original algorithm to make it compatible with the wireless module.

One of the first methods explored to optimize the algorithm was to zero-pad the vibration data to higher exponentials of two ( $2^n$ ). Three zero-padding cases were examined that allowed for a finer frequency-bin resolution; these were: 16,384 points, 32,768 points, and 65,536 points. Results indicate that zero-padding beyond the 16,384 data points does not meaningfully warrant the additional computation time associated with a larger data set. Hence, it was concluded that zero-padding the one-second sample data collected by the wireless sensor module to 16,384 data points was the most efficient and effective method in identifying the correct defect type and defect certainty (as measured by the NDE “max/sum” percentage).

Since side lobes are usually an undesired side effect of zero-padding, applying a Hanning window function to the vibration data was done to examine if the side lobes in the frequency spectrum were a concern. However, it was determined that applying a Hanning window only worsened the identification of the correct defect type and defect certainty. Based on this finding, it was decided not to employ a Hanning window function in this study.

Another approach utilized to improve the Level 2 analysis was to modify the hunting and integration ranges for medium (350 – 610 RPM or 60 – 105 km/h) and high (> 610 RPM or > 105 km/h) speeds. The hunting range ( $h_r$ ) provides a suitable window for the algorithm to search and identify the correct defect frequencies, while the integration range ( $i_r$ ) is used to capture the total area under the harmonics of the defect frequencies. Both of these calculations are a function of the frequency-bin resolution ( $r_s$ ). The optimal hunting and integration ranges that were chosen for medium and high speeds based on the results of this study were  $h_r = \pm r_s \times 8$  and  $i_r = \pm r_s$ , respectively. Using larger hunting ranges will most likely yield an incorrect defect frequency identification, while utilizing larger integration ranges will most probably lead to the capture of unwanted vibration energy from adjacent frequencies, thus resulting in an inaccurate Level 2 analysis in both cases. The optimal hunting and integration ranges determined by this study markedly improved the accuracy and reliability of the Level 2 analysis for the wireless sensor module. However, the absence of a suitable noise filter in the wireless module coupled with the effects of using only a one-second sample window results in noise being introduced throughout the frequency spectrum. This noise somewhat limited the effectiveness of the optimal hunting and integration ranges.

Modifications to the NDE calculations were done to mitigate the noise interference in the frequency spectrum that can affect the accuracy of the Level 2 analysis. Instead of summing the

areas under all harmonics for a given frequency range and dividing the total area by the number of harmonics for each fundamental defect frequency in that same frequency range, the average area for the first nine harmonics of each defect frequency were calculated. This modification allowed the defect type to be correctly identified 100% of the time under a full railcar operating condition. In contrast, the correct defect type is sometimes falsely identified under unloaded operating conditions (i.e., an empty railcar), but this is not a concern since spalls do not usually propagate when railcars are empty [24].

Although the identification of the correct defect type is much more accurate with the abovementioned optimizations, the defect percent certainty of the highest NDE for some instances remained slightly below the 50% criterion even though the defect type was correctly identified. Lower percentages can be perceived negatively and prompt the user reading the Level 2 analysis to be less confident with the outcome of the results. To improve the optics of this analysis, every NDE is cubed prior to dividing the highest NDE by the sum of the three NDEs. Certainty percentages of the highest NDE that might be slightly below 50% will now meet the 50% criterion while further differentiating the certainty percentages from the other two defect types. One downside to this approach is that the NDE percentages of incorrectly identified defect types can also be inflated leading to a false positive. However, the latter case is very rare and not a concern for bearings operating under full load conditions.

Several conclusions were made about the accuracy and reliability of the wireless sensor module. In general, increasing the load has a more pronounced effect on raising the defect percent certainty than increasing the operating speed. Defects on the same side of the bearing as the wireless sensor module (i.e., outboard location) result in higher defect certainties than inboard side defects. Furthermore, defects on the inboard side have much better defect certainties

under full railcar conditions. Although the optimized algorithm has been proven to correctly identify both cup and cone defects, the detection of cup defects is more accurate and reliable than the detection of cone defects. Finally, the optimized algorithm for implementation with the wireless sensor module that utilizes one-second sample windows collected at a sampling rate of 5200 Hz can also correctly identify roller defects.

Overall, the optimizations implemented to the defect detection algorithm allowed for an accurate and reliable assessment of the bearing condition and the characterization of the defective component. While the wireless sensor module did not achieve the same level of accuracy as the wired sensor module, the optimized algorithm for wireless utilization is five times faster than the original algorithm used with the wired sensor module. A shorter run-time of the algorithm will consume less computational power which will maximize the lifetime of the battery. Appendix A gives the optimized defect detection algorithm for the wireless sensor module, and Appendix B provides the original defect detection algorithm.

## REFERENCES

- [1] J. Cline, A. Bonetto, Cline, J., A. Bonetto, and T. Sultana. "Evaluation of hot bearing detector technology used to identify bearing temperatures." *Technology Digest* (2014).
- [2] C. Tarawneh, J. A. Turner, B. M. Wilson, and L. Koester\*. Service life testing of railroad bearings with known subsurface inclusions detected with advanced ultrasonic technology. *Int. J. of Railway Technology*, Vol. 2, No. 3, pp. 55-78, 2013.
- [3] C. Tarawneh, L. Koester\*, A. J. Fuller, B. M. Wilson, and J. A. Turner. Service life testing of components with defects in the rolling contact fatigue zone. *ASTM International*, STP 1548, West Conshohocken, PA, pp. 67-83, 2012.
- [4] Anderson, Gerald B. "Acoustic detection of distressed freight car roller bearings." *ASME/IEEE 2007 Joint Rail Conference and Internal Combustion Engine Division Spring Technical Conference*. American Society of Mechanical Engineers Digital Collection, 2007.
- [5] Author Federal Railroad Administration. (n.d.). *An Implementation Guide for Wayside Detector Systems*. Retrieved August 12, 2020, from <https://railroads.dot.gov/elibrary/implementation-guide-wayside-detector-systems>.
- [6] Hongru. (n.d.). Retrieved August 11, 2020, from <http://www.cccme.org.cn/products/detail-8196521.aspx>.
- [7] RailBAM: Bearing Acoustic Monitor. (n.d.). Retrieved August 12, 2020, from <http://www.trackiq.com.au/RailBAM.html>.
- [8] NATIONWIDE WAYSIDE DETECTOR SYSTEM. (n.d.). Retrieved August 12, 2020, from <https://docplayer.net/17829351-Nationwide-wayside-detector-system.html>.
- [9] Solution Details. (n.d.). Retrieved August 12, 2020, from <https://railadvisor.com/products/railbamregbearingacousticmonitor>.
- [10] Karunakaran, S., Snyder, T.W., 2007, "Bearing temperature performance in freight cars," *Proceedings Bearing Research Symposium*, sponsored by the AAR Research Program in conjunction with the ASME RTD Fall Conference, Chicago, IL, September 11-12.
- [11] C. Tarawneh, J. Aranda, V. Hernandez, S. Crown and J. Montalvo. "An investigation into wayside hot-box detector efficacy and Optimization," *International Journal of Rail Transportation*, under review, submitted March 2019.



- [12] J. Aranda, "Radiative Heat Transfer Analysis of Railroad Bearings for Wayside Thermal Detector Optimization," Master's Thesis, Department of Mechanical Engineering, The University of Texas Rio Grande Valley, December 2018.
- [13] A. Mealer, C. Tarawneh, S. Crown, Radiative Heat Transfer Analysis of Railroad Bearings for Wayside Hot-box Detector Optimization. Proceedings of the 2017 Joint Rail Conference, Philadelphia, PA, April 4-7, 2017.
- [14] 3.10 – Accident Causes | Federal Railroad Administration, Office of Safety Analysis. Web. <https://safetydata.fra.dot.gov/OfficeofSafety/publicsite/Query/inccaus.aspx>.
- [15] Government of Canada, T. (2017, April 11). Railway Investigation Report R11T0034. Retrieved August 27, 2020, from <https://www.tsb.gc.ca/eng/rapports-reports/rail/2011/r11t0034/r11t0034.html>
- [16] Government of Canada, T. (2017, April 10). Railway Investigation Report R11T0016. Retrieved August 30, 2020, from <https://www.tsb.gc.ca/eng/rapports-reports/rail/2011/r11t0016/r11t0016.html>
- [17] N. De Los Santos, R. Jones, C. Tarawneh, A. Fuentes, and A. Villarreal, 2017. "Development of prognostic techniques for surface defect growth in railroad bearing rolling elements." Proceedings of the 2017 ASME Joint Rail Conference, Philadelphia, PA, April 4-7.
- [18] A. Gonzalez, "Development, Optimization, and Implementation of a Vibration Based Defect Detection Algorithm for Railroad Bearings," Master's Thesis, The University of Texas Rio Grande Valley, August 2015.
- [19] J. Montalvo, 2019. "Defect detection algorithm optimization for use in freight railcar service." Master's Thesis, Mechanical Engineering Department, University of Texas Rio Grande Valley.
- [20] C. Tarawneh, J. A. Kypuros, B. Wilson, T. W. Snyder, A. A. Fuentes and B. A. Gonzalez, "A Collaborative On-Track Field Test Conducted to Verify the Laboratory Findings of Bearing Temperature Trending," in ASME Joint Rail Conference, Pueblo, CO, 2009.
- [21] I. L. Alvarado, "Defect Detection in Railroad Tapered-Roller Bearings using Vibration Analysis Techniques," Master's Thesis, University of Texas-Pan American, Edinburg, TX, 2012.
- [22] J. D. Lima, 2020. "Residual Service Life Prognostic Models for Taper Roller Bearings." Master's Thesis, Mechanical Engineering Department, University of Texas Rio Grande Valley.
- [23] National Instruments. (n.d.). Understanding FFTs and Windowing [PDF].

- [24] C. Tarawneh, J. Lima, N. De Los Santos, and R. Jones, 2019. "Prognostics models for railroad tapered-roller bearings with spall defects on inner or outer rings." *Tribology Transactions*, Vol. 62, No. 5, pp. 897-906.  
<https://doi.org/10.1080/10402004.2019.1634228>

## APPENDIX A

## APPENDIX A

### OPTIMIZED DEFECT DETECTION ALGORITHM FOR WIRELESS IMPLEMENTATION MATLAB CODE

```
%% Experiment Information

clearvars; %close all; clc;
answerstring = char(newid('Experiment: ', 'Supply the following info.',1));
answer1 = newid('Name:', 'Output File',1,{'Exp' answerstring
'WirelessVibrationInformation'});
StorePath = ['C:\Users\Jonas Cuanang\Desktop\UTRGV\Graduate
Research\Experiments\' answerstring '\Wireless Module\Zero Pad'];

if exist(StorePath, 'dir') == 0
    mkdir(StorePath);
end

%% Parameter Set Up
pp = 1600; % cutoff frequency for defect energy calculation
droller = 0.8425; % diameter of a Class F/K roller
rcone = 3.578367; % radius of a Class F/K cone
rcup = 4.408067; % radius of a Class F/K cup
locat = {'OB-SA'};

%% Integration Parameters
sbs = 1;
SR = 5200;
SL = floor(SR*sbs);

NFFT = 2^(nextpow2(SL)+1); % (zero pad) finds next even power of sample
length to properly pad for fft
res = SR/NFFT;

rmsvalue1 = [];
k = [];

%% Vibration Analysis
DataPath = ['C:\Users\Jonas Cuanang\Desktop\UTRGV\Graduate
Research\Experiments\' answerstring '\Wireless Module\'];
da = dir(DataPath);
ga = {da.name};
exp = char(answer1);
delete([exp '.xls']);
qf = regexp(ga, '_');
index = cellfun(@(x) length(x)==2, qf);
```

```

ga = ga(index);

if length(ga) >= 10
    ga = [ga(10:length(ga)) ga(1:9)];
end

progress = (1/length(ga));

ix = cellfun(@(x) regexp(x, '_'), ga, 'UniformOutput', 0);
ax = cellfun(@(x) x(1), ix);
temp2 = zeros(length(ga), 1);

for qqf = 1:length(ga)
    temp = ga(qqf);
    temp2(qqf, 1) = str2double(temp{1}(1:ax(qqf)-1));
end

temp3 = [temp2 (1:length(temp2))'];
temp3 = sortrows(temp3);
ga = ga(temp3(:, 2));

progressbar('Parsing through all speeds and loads...');

count = 0;

for i = 1:length(ga)

    p = [DataPath ga{i}];
    d = dir([p '\F*']);
    %changes working directory so selected folder and extracts all data files
    n = length(d);
    %counts the number of files in directory that are data files
    check = regexp(p, '_');
    check2 = regexp(p, '\');
    rpm = p(check(2)+1:length(p));
    rpm = str2double(rpm);
    percent = p(check(1)+1:check(2)-1);
    sheet = [num2str(percent) '_' num2str(rpm)];
    PrelimThsd = 0.004879*rpm-.09059;
    %Amy's thresholds
    MaxThsd = 0.0119*rpm-1.008;
    foldername = p(check2(9)+1:length(p));

    %% Level 2 Analysis Parameters

    %     if rpm > 610
    %         hunt = res*13;
    %         intrange = res*1;
    %     elseif rpm > 350 && rpm < 610
    %         hunt = res*19;
    %         intrange = res*1;
    %     elseif rpm > 240 && rpm < 350
    %         hunt = res*17;
    %         intrange = res*1;
    %     else

```

```

%         hunt = res*15;
%         intrange = res*1;
%     end

    if rpm > 610
        hunt = res*8;
        intrange = res*1;
    elseif rpm > 350 && rpm < 610
        hunt = res*8;
        intrange = res*1;
    elseif rpm > 240 && rpm < 350
        hunt = res*17;
        intrange = res*1;
    else
        hunt = res*15;
        intrange = res*1;
    end

    %% Tentative Frequencies
    wt = zeros(1,6);
    wt(1) = rpm/60;
Cone
    wt(2) = (rcone/(rcone+rcup))*wt(1);
Cage
    wt(3) = (rcone/droller)*wt(1);
Roller
    wt(4) = wt(2)*23;
Outer defect (cup)
    wt(5) = 23*(wt(1)-wt(2));
Inner defect (cone)
    wt(6) = (rcup/(droller/2))*wt(2);
Roller defect% loops through each sample window

    defectenergy1 = zeros(3,1,length(ga));
    T1 = zeros(length(ga),1);
    rmsvalue1 = zeros(n,1);

    %% Parses all the files and calculates both FFT and PSD
    defects = {'\omega_{cone}' '\omega_{cage}' '\omega_{roller}'...
              '\omega_{out}' '\omega_{in}' '\omega_{rolldef}'};

    for q = 1:n
%loops through all of the files

        file = fullfile(p,d(q).name);
%extracts file name
        rawdata = dlmread(file);
        acceldata = rawdata(1:5200,2);

        for lengt = 1:length(acceldata)

            if acceldata(lengt) > 0
                acceldata(lengt) = acceldata(lengt) + 1;
            elseif acceldata(lengt) < 0
                acceldata(lengt) = acceldata(lengt) + 1;
            end
        end
    end
end

```

```

        end
    end

    data = zeros(NFFT,1);
    data(1:length(acceldata)) = acceldata - mean(acceldata);
    x = data(1:length(acceldata)) - mean(data(1:length(acceldata)));
    rmsvalue1(q) = rms(x);
    rmsv = mean(rmsvalue1(3:length(rmsvalue1)));

    x = reshape(x,length(x),1);

    fftx = fft(x,NFFT);
%calculates fourier transform
    cutoff = ceil((NFFT+1)/2);
%finds the cutoff point
    fftx = fftx(1:cutoff,:)/NFFT;
%fft is symmetric, so we throw away half
    fftx = 2*mean(abs(fftx),2);
%then we scale
    psd(:) = fftx.^2;

    m = psd(:);
    f = SR/2*linspace(0,1,NFFT/2+1);
%calculates frequency vector
    f = f(1:cutoff)';
%throws away half

    totalPSD = sum(psd);

    rie = mean(diff(f));

    for ii = 1:length(wt)

        a = f>(wt(ii)-hunt) & f<(wt(ii)+hunt);
        [~,ind] = max(m(a)); %index of highest point
in range
        start = min(f(a));
        ind1 = f == start;
        [~,b] = max(ind1);
        w(ii) = f(ind+b-1); %corresponding
frequency of highest point
        w1{ii} = 0:w(ii):pp; %harmonics of found
frequency

        mag1 = 0; %initializes sum of magnitudes

        if ii > 3 %only does this part for the defect
frequencies

            z = w1{ii}; %copies harmonics into temporary
variable
            z = z(2:length(z)); %throws out the first number of
array as it will always be 0

```

```

for qq = 1:9 %loops through each harmonic

    index = f>(z(qq)-inrange) & f<(z(qq)+inrange);
    psd1=psd(:)';

    R1 = sum(psd1(index))/rie;
    mag1 = mag1 + R1;

end

defectenergy1(ii-3,1,q) = mag1/length(z);

end

T1(q) = trapz(f,psd(:));
tebar1 = mean(T1);

end

progressbar(progress*(i-1)+progress/n*(q-1)+progress/n);
indexpsd = f <= pp;
psd1 = psd(:,indexpsd)';

end

defectenergybar1 = (sum(defectenergy1,3)/n).^3; %cubed method
ps = max(defectenergybar1)./sum(defectenergybar1)*100;

defects = [{'Cup'} {'Cone'} {'Roller'}];
[~, defectindex] = max(defectenergybar1);

defects1 = defects(defectindex);

crmsv = num2cell(rmsv);
ctebar1 = num2cell(tebar1);
cdefectenergybar1 = num2cell(defectenergybar1);
cps = num2cell(ps);

excel = [{'Folder'} {foldername} {''} {''} {''}; {'Percent Load'}
{percent} {''} {''} {''};...
{'RPM'} {rpm} {''} {''} {''}; {''} locat {''} {''} {''}; {''} {''}
{'RMS'} {'Value'} {''}; {''} crmsv {''} {''} {''};...
{''} {''} {'Total'} {'Energy'} {''}; {''} ctebar1 {''} {''} {''}; {''}
locat {''} {''} {''}; {''} {''} {'Defect'} {'Energy'} {''};...
{'Cup'} cdefectenergybar1(1) {''} {''} {''}; {'Cone'}
cdefectenergybar1(2) {''} {''} {''}; {'Roller'} cdefectenergybar1(3) {''}
{''} {''};...
{'Percent'} cps {''} {''} {''}; {''} defects1 {''} {''} {''}];%; {''}
{''} {''} {''} {''}; {'Kurtosis='} ckurt; {'Crest Factor='} cCrestFactor];

xlswrite([StorePath '\\' exp], excel, 'root', ['A'
num2str((count)*20+1)]);

```



```
    xlswrite([StorePath '\\' exp], [{foldername} {percent} {rpm} crmsv
{PrelimThsd} {MaxThsd} {foldername} {rpm} cps(1) defects1{1}], 'root2', ['A'
num2str((count)+1)]);

    mm = length(rmsvalue1);
    nn = length(k);
    k(nn+1:mm+nn) = rmsvalue1;

    count = count+1;

    progressbar(progress*i/length(sbs));

    rmsvalue1 = [];

end
```

## APPENDIX B

## APPENDIX B

### ORIGINAL DEFECT DETECTION ALGORITHM MATLAB CODE

```
%% Experiment information
clearvars; close all; clc;
answer = newid('Experiment: ', 'Supply the following info.',1);
answer6 = questdlg('Is this for the SBT or 4BT?', 'Supply the following
info.','SBT','4BT','4BT');
answerstring = char(answer);
answer1 = newid('Name:', 'Output File',1,{'Exp' answerstring
'VibrationInformation'});
accel = 4;
sbs = 4;
count = 0;

switch answer6
    case 'SBT'
        locat = {'IB-SA' 'IB-M' 'OB-SA' 'OB-M'};
        SR = 1/0.000180;
        SL = floor(SR*sbs);
    case '4BT'
        locat = {'B2-SA' 'B2-M' 'B3-SA' 'B3-M'};
        SR = 5120;
        SL = floor(SR*sbs);
end

%% Parameter set up
pp = 1000; %
cutoff frequency for defect energy calculation %
droller = 0.8425; %
diameter of a Class F/K roller %
rcone = 3.578367; %
radius of a Class F/K cone %
rcup = 4.408067; %
radius of a Class F/K cup

%% Integration parameters
psdcalc = 1;
pad = 1;
differential = 1;
inttype = 1;

if pad == 1
    NFFT = 2^(nextpow2(SL));
%finds next even power of sample length to properly pad for fft
else
    NFFT = 2^(nextpow2(SL)-1);
end
```

```

path = ['C:\Users\Jonas Cuanang\Desktop\UTRGV\Graduate Research\Experiments\'
answerstring '\ADXL\'];
path2 = ['C:\Users\Jonas Cuanang\Desktop\UTRGV\Graduate
Research\Experiments\' answerstring '\ADXL\Zero Pad 4 sbs'];
if exist(path2,'dir') == 0
    mkdir(path2);
end
da = dir(path);
ga = {da.name};
exp = char(answer1);
delete([exp '.xls']);
q = regexp(ga, '_');
index = cellfun(@(x) length(x)==2, q);
ga = ga(index);
if length(ga) >= 10
    ga = [ga(10:length(ga)) ga(1:9)];
end

progress = (1/length(ga));

ix = cellfun(@(x) regexp(x, '_'), ga, 'UniformOutput', 0);
ax = cellfun(@(x) x(1), ix);
temp2 = zeros(length(ga), 1);
for qq = 1:length(ga)
    temp = ga(qq);
    temp2(qq, 1) = str2double(temp{1}(1:ax(qq)-1));
end
temp3 = [temp2 (1:length(temp2))'];
temp3 = sortrows(temp3);
ga = ga(temp3(:, 2));

progressbar('Parsing through all speeds and loads...');

for i = 1:length(ga)
    p = [path ga{i}];
    d = dir([p '\70gAccelerometerData*.lvm']);
    %changes working directory so selected folder and extracts all lvm files
    n = length(d);
    %counts the number of files in directory that are lvm files
    check = regexp(p, '_');
    check2 = regexp(p, '\');
    rpm = p(check(2)+1:length(p));
    rpm = str2double(rpm);
    percent = p(check(1)+1:check(2)-1);
    sheet = [num2str(percent) '_' num2str(rpm)];
    PrelimThsd = 0.004879*rpm-.09059;
    MaxThsd = 0.0119*rpm-1.008;
    foldername = p(check2(9)+1:length(p));

    res = SR/NFFT;
    if rpm > 610
        hunt = res*15;
        intrange = res*3;
    elseif rpm > 350 && rpm < 610
        hunt = res*10;
    end
end

```

```

    intrange = res*3;
elseif rpm > 240 && rpm < 350
    hunt = res*8;
    intrange = res*3;
else
    hunt = res*6;
    intrange = res*3;
end

%% Tentative frequencies
wt = zeros(1,6);
wt(1) = rpm/60; %
Cone
wt(2) = (rcone/(rcone+rcup))*wt(1); %
Cage
wt(3) = (rcone/droller)*wt(1); %
Roller
wt(4) = wt(2)*23; %
Outer defect (cup)
wt(5) = 23*(wt(1)-wt(2)); %
Inner defect (cone)
wt(6) = (rcup/(droller/2))*wt(2); %
Roller defect% loops through each SW
%% Set up variables
CrestFact = zeros(n,accel); rmsvalue = zeros(n,accel);
defectenergy1 = zeros(3,accel,length(ga)); kurt1 =
zeros(length(ga),accel);
T1 = zeros(length(ga),accel);

%% Parses all the files and calculates both FFT and PSD
for q = 1:n
%loops through all of the files
file = fullfile(p,d(q).name);
%extracts file name
l = length(file);
%finds length of file name
rawdata = dlmread(file,'\t',[23 0 SL+22 4]);
rawdata = rawdata(1:floor(SL),:);
rawdata(:,2:3) = rawdata(:,2:3) + 0.02; %adds 1G to new ADXLs

if q == 1
    if exist([p '\Sensitivity'],'dir')
        rpath = [p '\Sensitivity'];
        dreset = dir([rpath '\Reset_70gAccelerometerData*.lvm']);
        creset = dir([rpath '\70gAccelerometerData*.lvm']);
        filereset = fullfile(rpath,dreset.name);
        filedc = fullfile(rpath,creset.name);
        rawreset = dlmread(filereset,'\t',24,0);
        rawresetc = dlmread(filedc,'\t',[23 0 SL+22 4]);
        datareset = rawreset(:,2:5);
        datadc = rawresetc(:,2:5);
        ss = (rms(datareset)-mean(datadc))./140;
    else
        ss = [.0242 .0242 .0242 .0242];
    end
end
end

```

```

        xx = zeros(accel,SL);
        for j = 1:accel
%loops for each accelerometer
            sensitivity = ss(j);
            data = zeros(NFFT,1);
            if differential == 1
                data(1:length(rawdata(:,j+1))) = 0.5*((rawdata(:,j+1) -
mean(rawdata(:,j+1)))/sensitivity);           %processes data for fourier
transform
                if j == 1 || j==2
                    data(1:length(rawdata(:,j+1))) = ((rawdata(:,j+1) -
mean(rawdata(:,j+1)))/.02);
                end
            else
                data(1:length(rawdata(:,j+1))) = (rawdata(:,j+1) -
mean(rawdata(:,j+1)))/sensitivity;           %processes data for fourier
transform
            end

            x = data(1:length(rawdata(:,j+1))) -
mean(data(1:length(rawdata(:,j+1))));
            rmsvalue(q,j) = rms(x);
            rmsv = mean(rmsvalue);
            CrestFactors(i,j) = max(abs(x))/rmsv(j);

            x = reshape(x,SL,1);
            CrestFact(q,j) = ((max(x)-min(x))/2)./rmsvalue(q,j);
%Calculates Crest Factor for each File
            xx(j,:) = x;

            if psdcalc == 1
                fftx = fft(x,NFFT);
%calculates fourier transform
                cutoff = ceil((NFFT+1)/2);
%finds the cutoff point
                fftx = fftx(1:cutoff,+)/NFFT;
%fft is symmetric, so we throw away second half
                fftx = 2*mean(abs(fftx),2);
%then we scale
                psd(j,:) = fftx.^2;
                m = psd(j,:);
                f = SR/2*linspace(0,1,NFFT/2+1);
%calculates frequency vector
                f = f(1:cutoff)';
%throws away half
            else
                Pxx = abs(fft(x,NFFT)).^2/length(x)/SR;
                Hpsd = dspdata.psd(Pxx(1:length(Pxx)/2),'Fs',SR);
                Hpsdm = 10.^(Hpsd.data./10)-1;
                Hpsdf = (Hpsd.frequencies);
                psd(j,:) = Hpsdm;
                m = Hpsdm;
                f(j) = Hpsdf;
            end
            rie = mean(diff(f));

```

```

        for ii = 1:length(wt)
%loops for each frequency
            a = f>(wt(ii)-hunt) & f<(wt(ii)+hunt);
            [~,ind] = max(m(a));
%index of highest point in range
            start = min(f(a));
            ind1 = f == start;
            [~,b] = max(ind1);
            w(ii) = f(ind+b-1);
%corresponding frequency of highest point
            w1{ii} = 0:w(ii):pp;
%harmonics of found frequency
            mag = 0;
%initializes sum of magnitudes
            mag1 = 0;
            if ii > 3
%only does this part for the defect frequencies
                z = w1{ii};
%copies harmonics into temporary variable
                z = z(2:length(z));
%throws out the first number of array as it will always be 0
                for qq = 1:length(z)
%loops through each harmonic
                    index = f>(z(qq)-inrange) & f<(z(qq)+inrange);

                    psd1=psd(j,:)' ;
                    if inttype == 1
                        R1 = sum(psd1(index))/rie;
                        mag1 = mag1 + R1;
                    else
                        R1 = trapz(f(index),psd1(index));
                        mag1 = mag1 + R1;
                    end

                    end
                    defectenergy1(ii-3,j,q) = mag1/length(z);
                    end
                    T1(q,j) = trapz(f,psd(j,:));
                    tebar1 = mean(T1);
                    end
                    progressbar(progress*(i-1)+progress/n*(q-1)+progress/n/accel*j);
                    end
                    indexpsd= f <= pp;
                    psd1=psd(:,indexpsd)';
                    kurt1(q,:) = kurtosis1(xx');
                end

            kurt = rms(kurt1);
            CrestFactor = rms(CrestFact);
            defectenergybar1 = (sum(defectenergy1,3)/n).^2;
            defectenergybar2 = (sum(defectenergy1,3)/n).^2;
            ps = max(defectenergybar1)./sum(defectenergybar1)*100;
            ps2 = max(defectenergybar2)./sum(defectenergybar2)*100;
%squaring method for higher confidence in defect component
            defects = [{'Cup'} {'Cone'} {'Roller'}];
            [~, defectindex] = max(defectenergybar1);

```

```

[~, defectindex2] = max(defectenergybar2);
defects1 = defects(defectindex);
defects3 = defects(defectindex2);
%   rmsv = mean(rmsvalue);
    crmsv = num2cell(rmsv); ctebar1 = num2cell(tebar1); cdefectenergybar1 =
num2cell(defectenergybar1);
    cps = num2cell(ps);
    ckurt = num2cell(kurt);
    cCrestFactor = num2cell(CrestFactors(i,:));
    cdefectenergybar2 = num2cell(defectenergybar2);
    cps2 = num2cell(ps2);
    %% Write Exp. Info to Excel
    excel = [{'Folder'} {foldername} {''} {''} {''}; {'Percent Load'}
{percent} {''} {''} {''};...
    {'RPM'} {rpm} {''} {''} {''}; {''} locat; {''} {''} {'RMS'} {'Value'}
{''}; {''} crmsv;...
    {''} {''} {'Total'} {'Energy'} {''}; {''} ctebar1; {''} locat; {''}
{''} {'Defect'} {'Energy'} {''};...
    {'Cup'} cdefectenergybar1(1,:); {'Cone'} cdefectenergybar1(2,:);
{'Roller'} cdefectenergybar1(3,:);...
    {'Percent'} cps; {''} defects1; {''} {''} {''} {''} {''};
{'Kurtosis='} ckurt; {'Crest Factor='} cCrestFactor];
    excel2 = [{''} locat; {''} {'Square'} {'Defect'} {'Energy'} {''};...
    {'Cup'} cdefectenergybar2(1,:); {'Cone'} cdefectenergybar2(2,:);
{'Roller'} cdefectenergybar2(3,:);...
    {'Percent'} cps2; {''} defects3;];
    xlswrite([path2 '\\' exp], excel, 'root', ['A' num2str((count)*20+1)]);
%   xlswrite([path2 '\\' exp], excel2, 'root', ['N' num2str((count)*20+9)]);
    xlswrite([path2 '\\' exp], [{foldername} {percent} {rpm} crmsv
{PrelimThsd} {MaxThsd} {foldername} {rpm} cps2(1) defects1{1} {foldername}
{rpm} cps2(2) defects1{2} {foldername} {rpm} cps2(3) defects1{3} {foldername}
{rpm} cps2(4) defects1{4}], 'root2', ['A' num2str((count)+1)]);

    count = count+1;
    progressbar(progress*i);
end
progressbar(1);

```



## BIOGRAPHICAL SKETCH

Jonas Cuanang was born in the Philippines on July 3, 1998. He later became a U.S. citizen in 2016. In May 2016, he obtained his high school diploma along with his associate degree in engineering at South Texas College. Afterwards, he graduated Magna Cum Laude with his bachelor's degree in Mechanical Engineering at the University of Texas Rio Grande Valley (UTRGV) in December 2018. On August 2018, Jonas began his education in mechanical engineering as a graduate student at UTRGV. He has received the Dwight David Eisenhower Transportation Fellowship and has a full ride for his graduate career with the help of the Presidential Graduate Research Assistantship. During this time at UTRGV, Jonas has been involved in numerous research projects involving nanotechnology and railway applications, where he has published several research papers and presented his findings at a conference. He completed his Master of Science degree in Mechanical Engineering in December 2020. Jonas Cuanang can be reached at [cuanjonas2@gmail.com](mailto:cuanjonas2@gmail.com).